

# Die Ausdehnung der Inverse-Compton-Komponente des Krebsnebels

## The Spatial Extension of the Inverse Compton Component of the Crab Nebula

Masterarbeit

im Fachbereich Physik

der Universität Hamburg

korrigierte Fassung vom 01.06.2016

Eingereicht von: Serge Rosen  
Institut: Institut für Experimentalphysik  
Arbeitsgruppe: Astroteilchenphysik



# Table of Contents

Zusammenfassung.....	3
Abstract.....	4
1 Introduction.....	1
2 The Crab.....	3
2.1 The Crab Pulsar:.....	4
2.2 The Crab Nebula:.....	5
2.3 Radiation Processes:.....	8
2.3.1 Synchrotron Radiation:.....	8
2.3.2 Inverse Compton Radiation:.....	9
2.4 Markarian 421:.....	12
3 Fermi LAT.....	14
3.1 Fermi LAT Components:.....	16
3.1.1 Precision Converter-Tracker:.....	17
3.1.2 Calorimeter:.....	20
3.1.3 Trigger and Anti-Coincidence Detector:.....	21
3.2 Data Format:.....	22
3.3 Fermi Tools:.....	24
4 Data Selection.....	26
4.1 Initial Data Set:.....	26
4.2 Simulations:.....	29
4.3 Applied Cuts:.....	31
5 Data Analysis:.....	40
5.1 Angular Separation of the Crab Nebula:.....	40
5.2 Angular Separation of Markarian 421:.....	45
5.3 Crab Minor and Major Axis:.....	54
6 Results and Outlook.....	59
Appendix.....	61
Appendix A.....	61
Appendix B.....	65
List of Figures.....	71
Bibliography.....	73



# Zusammenfassung

Diese Masterarbeit untersucht die Ausdehnung des Krebsnebels in Energiebereichen, in denen die Inverse-Compton-Komponente seines Strahlungsspektrums dominiert. Die Größe des Inverse-Compton-Krebsnebels wurde auf den Radius  $0.040^\circ$  bestimmt, mit einem 95%-Konfidenzintervall von  $0.035^\circ$  bis  $0.050^\circ$ . Die Hypothese des Inverse-Compton-Krebsnebels als Punktquelle wurde mit einem Signifikanzwert von  $p < 10^{-4}$  ausgeschlossen. Ferner wurde die Ausdehnung des Krebsnebels entlang seiner Haupt- und Nebenachsen bei denselben Energien vermessen. Diese wurden auf die Radii  $0.045^\circ$ , bzw.  $0.040^\circ$  bestimmt, mit einem 95%-Konfidenzintervall von  $0.030^\circ$  bis  $0.050^\circ$ , respektive  $0.020^\circ$  bis  $0.045^\circ$ . Eine Überprüfung der Analysemethoden anhand der Referenzquelle Markarian 421 wurde durchgeführt. Diese konnte Markarian 421 nicht als Punktquelle reproduzieren.

# Abstract

This Master's thesis examines the spatial extension of the Crab nebula in energy ranges, in which the inverse Compton component of its spectrum dominates. The size of the inverse Compton Crab nebula was determined to be of radius  $0.040^\circ$ , with a 95% confidence interval ranging from  $0.035^\circ$  to  $0.050^\circ$ . The hypothesis of a pointlike inverse Compton Crab nebula could be excluded with a significance of  $p < 10^{-4}$ . Additionally, the extension of the Crab nebula along its major and minor axes was measured at the same energies. They were determined to be of radii,  $0.045^\circ$  and  $0.040^\circ$ , with 95% confidence intervals from  $0.030^\circ$  to  $0.050^\circ$  and  $0.020^\circ$  to  $0.045^\circ$  respectively. A cross check of the analysis process was performed on the reference source Markarian 421. This analysis could not reproduce Markarian 421 as a point source.

# 1 Introduction

Photons travel on geodesics. Specifically, they do not interact with magnetic fields as charged cosmic rays do, meaning they do not get refracted on their way to earth. The ability to determine their source is solely limited by one's ability to reconstruct its incoming direction. They provide the most universal insight to all astronomical objects, and for the most of human history, the study of stars was equivalent to the study of photons from the night sky. As photons are created through the interaction of charged particles, they even provide information about other particle types, and in many ways, help us gain a deeper understanding of astrophysics and the universe.

The high-energy gamma-ray sky is the upper energy boundary in the study of astronomical photons. It provides a direct link to the most energetic particle interactions in the known universe, and could potentially reveal the open question of the source of cosmic rays. Through the use of ever larger and ever more advanced detectors, more and more gamma-ray sources have been identified, and the study of these sources remains a field of high interest.

The Crab pulsar and its adjoining nebula have long been a staple of both pulsar physics as well as gamma-ray physics. Many phenomena of pulsars and pulsar wind nebulae have first been discovered in the Crab, with potentially many more to be revealed yet. As a source that is both exceptionally bright and exceptionally stable, it has become a gateway to the understanding of the high-energy gamma-ray sky, so much so, that the flux of other very high-energy gamma-ray objects are commonly measured in units of Crab flux.

At gamma-ray energies, the Crab nebula's properties have changed significantly from that of the radio Crab nebula. The biggest change is the change in the dominant radiative process through which it generates very high-energy gamma-rays. While from radio to high-energy gamma-rays most of the Crab nebula's emission stem from synchrotron radiation, at very-high energies a new spectral component, the inverse Compton component, which had previously been al-

# **The Spatial Extension of the Inverse Compton Component of the Crab Nebula**

## *1 Introduction*

---

most completely suppressed, takes over. At these energies, the inverse Compton radiation could provide insights about the Crab nebula which had been completely inaccessible before.

The aim of this Master's thesis is to take a look at the extension of the Crab nebula at energies where the inverse Compton part of its spectrum starts to dominate. At these energies, the synchrotron component is reduced in size to an almost pointlike source, while the inverse Compton component is expected to be emitted uniformly by the entire nebula. By comparing its extension to that at radio energies, it may even be possible to see an otherwise cold electron population that may have played a pivotal part in the formation of the nebula.

## 2 The Crab

The descriptions in this chapter are largely adopted from Bühler & Blandford (2014).

The Crab nebula is a pulsar wind nebula located within the constellation of Taurus. It is a product of the “first historical supernova” (Bühler & Blandford 2014, p.3), which can be dated precisely to the 25<sup>th</sup> of August 1054 A.D. Aside from the nebula (figure 2.1), the other major remnant of the same supernova is the Crab pulsar located within the nebula, often collectively referred to as “the Crab”.

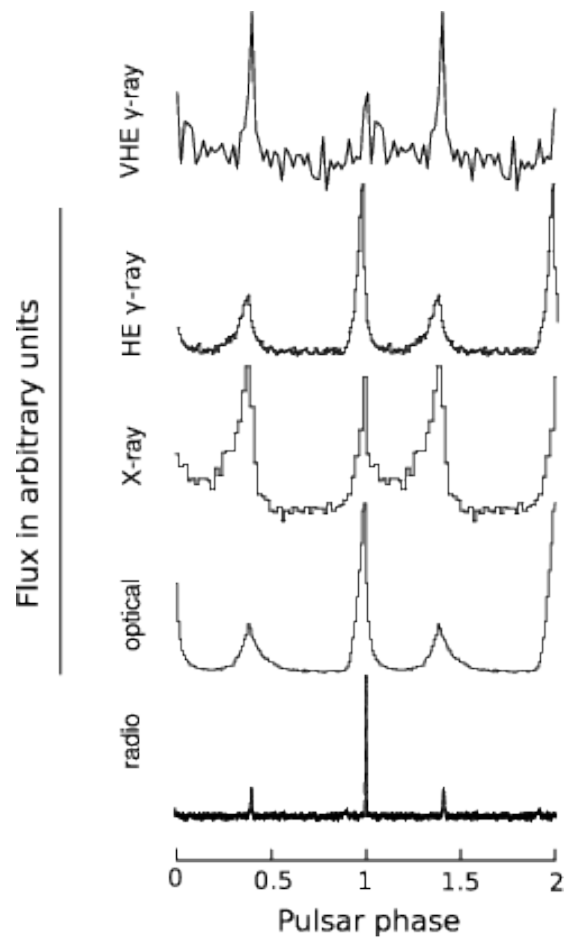
Due to its high luminosity and its relative proximity of 2 kpc, the Crab has been thoroughly studied, leading to an extended understanding of non-thermal processes in the universe. For instance, pulsed optical emission have first been observed in the Crab before they were found in other sources (Cocke, Disney & Taylor 1969). Major discoveries regarding the Crab are frequently made to this day. Only recently, very-high-energy gamma-ray emission ( $E > 100$  GeV) have been detected in the Crab pulsar (Aleksic et al. 2012), as well as high-energy gamma-ray flares ( $E > 100$  MeV) (Tavani et al. 2011), two things never before observed in other pulsar wind nebulae.

This section describes the Crab and in particular the Crab nebula as the object of study for this thesis. First, this chapter gives a full description of the properties of the Crab nebula, followed by a full description of the Crab pulsar. Then it introduces the main processes through which the Crab produces high-energy photons, namely synchrotron and inverse Compton radiation. Lastly, this chapter describes Markarian 421, an extragalactic point source on which a cross check of the analysis process can be performed.

# The Spatial Extension of the Inverse Compton Component of the Crab Nebula

## 2 The Crab

---



# The Spatial Extension of the Inverse Compton Component of the Crab Nebula

## 2 The Crab

---

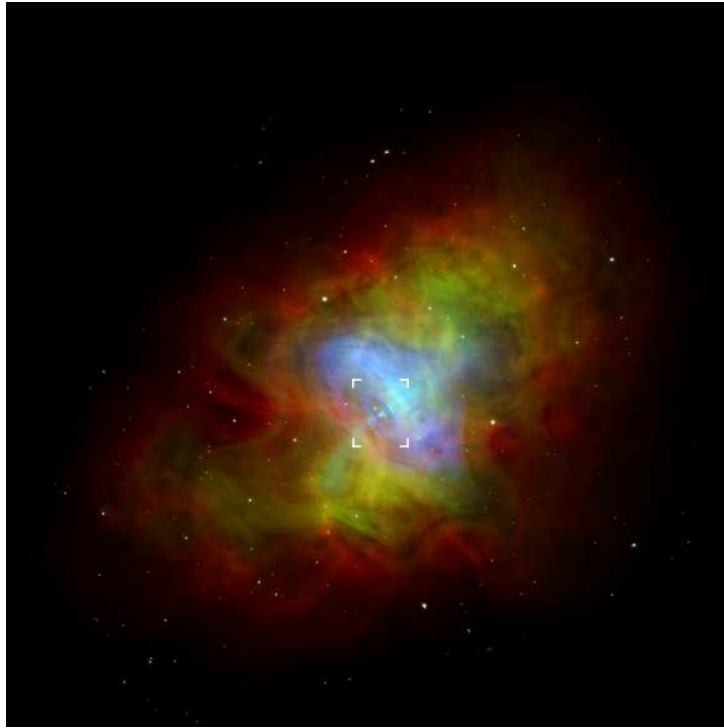


**Figure 2.1:** A composite image of the Crab nebula at different energies. Radio emissions are depicted in red, optical emissions in green, and X-ray in blue. The shape is roughly that of an ellipsis tilted relative to the earth's axis. It is visible how the Crab nebula's emission region gets smaller with increasing energy. (Bühler & Blandford 2014)

## 2.1 The Crab Pulsar:

The Crab pulsar (Bühler & Blandford 2014) is a pulsar located at  $05^{\text{h}} 34^{\text{m}} 31.97^{\text{s}}$  right ascension and  $+22^{\circ} 00' 52.1''$  declination. Pulsars are possible products of supernovae. At the end of its life cycle, a star may erupt in a supernova explosion, in which the gravitational pull on the star's interior overcomes the radiation pressure produced by nuclear fusion. The remnant of such an explosion is a neutron star, containing most of the original star's mass confined in a sphere with a radius of only a few kilometers. This has some drastic effects on its properties. Because of conservation of momentum and energy, the neutron star retains its angular momentum and its squared magnetic energy density, leading to very low rotation periods and strong magnetic fields. Since the magnetic and rotational poles usually aren't aligned, the magnetic field rapidly changes

# The Spatial Extension of the Inverse Compton Component of the Crab Nebula

## 2 The Crab

---

upon rotating and emits strongly collimated radiation. As the star rotates, these emissions pass the field of view of earth for short times. The emissions thereby appear to be pulsed, and such a star is called a pulsar (Harding 2013).

The Crab pulsar has a pulsation period of roughly 33.6 ms, which is slowing down at a rate of  $4.2 \cdot 10^{-13}$ . This slow-down rate, however, is prone to glitches, limited time frames in which the slow-down rate massively increases or decreases. Because of this, ephemerides are needed, which are tables keeping a steady track of the pulsation period and the slow-down rate for a pulsar at specific points in time. Otherwise, the error in the pulse timing would pile up and create the illusion of a (more) uniform distribution throughout the pulsar phase. An unusual characteristic of the Crab pulsar is the occurrence of flares, where over short periods of time, the flux of radio emissions increases hundred- or even thousandfold.

Like the majority of high-energy pulsars, the Crab pulsar has two peaks (figure 2.2) in its phase profile. The main pulse is located at the pulsar phase  $\phi = 0.0/1.0$  and the inter-pulse at  $\phi = 0.4$  (Bühler & Blandford 2014). Throughout different energy bands, only shifts smaller than  $\Delta\phi < 0.01$  in their arrival times are seen. Its spectrum mainly consists of three components: a radio component, an X-ray component, and a gamma-ray component emerging at energies greater than 100 MeV.

## 2.2 The Crab Nebula:

The Crab nebula is a pulsar wind nebula. It is part of a system which can be divided into three parts: the pulsar and its magnetosphere, the cold pulsar wind, and the synchrotron nebula. As only about 10% of the rotational energy lost by the Crab pulsar is lost in pulsed emission, it is believed the rest flows into the construction of its nebula. Pulsar wind nebulae are created when, at the

# The Spatial Extension of the Inverse Compton Component of the Crab Nebula

## 2 The Crab

---

**Figure 2.2:** Crab flux as a function of the pulsar phase over two pulsation periods. The individual pictures refer to the energy ranges radio (1.4 GHz), optical (1.5 – 3.5 eV), x-ray(100 – 200 keV), high-energy gamma-ray (100 - 300~MeV), ultra-high-energy gamma-ray (50 – 400 GeV). (Bühler & Blandford 2014)

pulsar surface, the strong rotating magnetic field induces a large electric potential. This potential is big enough to rip particles out of the pulsar and fill its magnetosphere with plasma, which then flows out and is accelerated along the magnetic field lines. This pulsar wind predominately consists of electrons (and in equal part positrons). The wind itself is radiationless, until it starts interacting with the nebula at the termination surface. In the case of the Crab, the termination surface is located at a distance of about 10 arcseconds from the pulsar. At this surface, the surrounding nebula's pressure causes the electrons to radiate, mostly through synchrotron radiation. It is also assumed that the electrons are reaccelerated at the termination surface as an additional acceleration to that at the field lines inside the pulsar wind. Three-dimensional simulations of the nebula development even suggest that no acceleration along the magnetic field lines is needed, and the particle acceleration is entirely done at the termination surface (Porth, Komissarov & Keppens, 2012). The properties of any individual pulsar wind nebula much depend on the properties of its pulsar.

The Crab nebula is roughly elliptical in shape, with a major axis of 7 arcminutes, and a minor axis of 4.6 arcminutes across, and an angle between major axis and right ascension of 30 degrees (Hester 2008). In optical, many substructures of the nebula can be seen, for example thin arcs of increased emission, called wisps, which give the nebula its crab-like appearance. These substructures disappear with increased energy, since the outer regions of the Crab emit a softer spectrum.

At lower energies, the nebula mostly emits synchrotron radiation. At energies higher than 1 GeV however, another spectral component starts to dominate, which is its inverse Compton component. Both will be more thoroughly explained in section 2.3.

Another noteworthy feature of the Crab nebula is the irregular appearance of flares, during which the gamma-ray flux of the Crab nebula dramatically increases up to a factor of  $\sim 30$ . Until

# The Spatial Extension of the Inverse Compton Component of the Crab Nebula

## 2 The Crab

---

September 2013, six high-energy flares have been recorded (Mayer et al. 2013, Tavani et al. 2011). The increase in flux and spectrum during the flare vary considerably. During the flare of April 2011, the largest of its kind, an entirely new spectral component was found (Bühler 2011). The origin of these high-energy flares still remains unclear.

## 2.3 Radiation Processes:

This chapter features a short description of synchrotron and inverse Compton radiation. A more thorough derivation of the properties of both synchrotron and inverse Compton radiation can be found in Appendix A.

### 2.3.1 Synchrotron Radiation:

When a charged particle is accelerated, it radiates electromagnetically. This is true regardless of the form of acceleration, be it an in- or decrease of the total particle momentum or deflection of the particle. It can be shown (Rybicki & Lightman 1979, p. 140) that the total radiated power is:

$$P = \frac{2q^2}{3c^3} \gamma^4 (a_{\perp}^2 + \gamma^2 a_{\parallel}^2)$$

with  $q$  the charge of the particle and  $\gamma = E/(mc^2)$  the Lorentz factor.

Magnetic fields deflect charged particles which have a velocity component perpendicular to them onto a circular path (or a spiral path in case of an additional parallel component). This deflection leads to the particle radiating light. In the case of a relativistic particle, this emitted radiation is referred to as synchrotron radiation, after synchrotron particle accelerators in which it was first discovered. It is one of the most common types of radiation in astrophysics, as it is

# The Spatial Extension of the Inverse Compton Component of the Crab Nebula

## 2 The Crab

---

present in all systems containing relativistic particles and magnetic fields. In the case of the Crab nebula, the emitting particles are electrons accelerated at the shock front of the Crab pulsar, which then interact with the nebula's ambient magnetic field.

The total power emitted by a single electron through synchrotron radiation is:

$$P = \frac{2q^2}{3c^3} \gamma^4 \frac{q^2 B^2}{\gamma^2 m^2 c^2} v_{\text{perp}} = \frac{2}{3} r_0^2 c \beta_{\text{perp}} \gamma^2 B^2$$

where  $r_0 = q^2/(4\pi\epsilon_0 mc^2)$  is the electromagnetic particle radius and  $\beta = v/c$ .

This emission is highly dependent on the particles' average Lorentz factor, so that lighter particles (i.e. electrons) radiate much stronger than heavier ones. This equation for the total emitted particle power can be rearranged as:

$$P = \left(\frac{2}{3}\right)^2 r_0^2 c \beta^2 \gamma^2 B^2 = \frac{4}{3} \sigma_T c \beta^2 \gamma^2 U_B$$

with the Thomson cross section as  $\sigma_T = 8/3 \pi r_0^2$  and the magnetic energy density  $U_B = B^2/8\pi$

The size of any synchrotron emission region is tied, on the one hand, to the distribution of its magnetic fields. On the other hand, it is also tied to the injection location of the emitting particles. As the particles emit synchrotron radiation, they lose energy and velocity, leading to a smaller Lorentz factor and weaker emissions. The mean free path  $\lambda_{1/2}$  for an electron over which it loses half of its energy due to synchrotron radiation is given by:

$$\lambda_{1/2} = \beta c t_{1/2} = \frac{\gamma}{|\dot{\gamma}|} \propto \gamma^{-1}$$

The mean free path drops off with increasing energy. In the case of high-energy gamma-rays for the Crab nebula, this mean free path becomes too short for the strongest synchrotron emission to occur too far from where the electrons are injected into the magnetic field. For the Crab nebula, this injection point is the shock front of the Crab pulsar, leading to the synchrotron nebula to appear pointlike at high energies (explaining the decrease in size in figure 2.1 with increasing photon energy).

# The Spatial Extension of the Inverse Compton Component of the Crab Nebula

## 2 The Crab

---

### 2.3.2 Inverse Compton Radiation:

The Compton effect occurs whenever a photon is scattered off an electron at rest. Since the photon carries momentum, the electron can recoil, gaining energy and momentum which the photon loses. The scattered photon therefore has higher wavelength and lower energy than the incoming one. The change in wavelength is always positive and is described by:

$$\lambda_1 - \lambda = \lambda_c (1 - \cos \theta)$$

Inverse Compton scattering

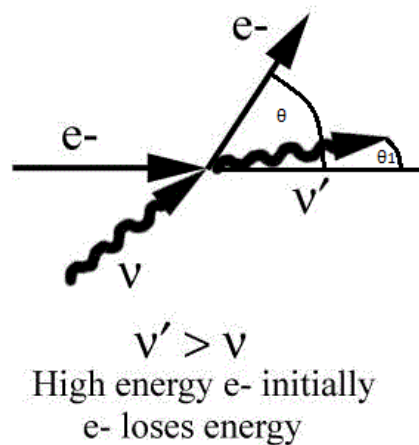


**Figure 2.3:** A sketch of the inverse Compton effect. The incoming photon is scattered off a highly relativistic electron and gains energy. ([venables.asu.edu/quant/proj/compton.html](http://venables.asu.edu/quant/proj/compton.html))

with  $\lambda$  the wavelength of the incoming and  $\lambda_1$  the wavelength of the outgoing photon, and the Compton wavelength defined as:

$$\lambda_c \equiv \frac{h}{mc}$$

For electrons, it is  $\lambda_c = 0.02426 \text{ \AA}$ .

In the rest frame of the electron, the Compton effect is always the same, and the energy transfer is always from the photon onto the electron. In a different reference frame (the lab frame)

# The Spatial Extension of the Inverse Compton Component of the Crab Nebula

## 2 The Crab

---

however, in which the electron is highly relativistic, the momentum transfer may slow down the electron, resulting in a net energy transfer from the electron to the photon. This case is called the inverse Compton effect. This process is commonplace in astrophysics and generates high-energy photons, which as a whole, are referred to as inverse Compton radiation.

The exact properties of the inverse Compton effect can be derived from the properties of the Compton effect by solving its equations in a Lorentz-boosted reference frame. This leads to the energy of the outgoing photon  $\epsilon_1$  in the case optimal angles to be:

$$\epsilon_1 = \frac{4\epsilon\gamma^2}{1 + \frac{2\epsilon\gamma}{mc^2}} \approx 4\epsilon\gamma^2$$

with  $\epsilon$  the energy of the incoming photon.

If  $\epsilon\gamma \ll mc^2$  holds, so does the approximation on the right-hand side. It is still a good approximation for photons of energies  $\sim 100$  keV scattered off electrons with a gamma of 1000. This way, the inverse Compton effect can easily generate photons with energies  $> 1$  GeV.

The total power emitted by a single through inverse Compton radiation by an arbitrary photon density can be derived to be:

$$P_{compt} = \frac{4}{3}\sigma_T c \gamma^2 \beta^2 U_{ph}$$

This emitted power has very similar dependencies on most factors to the emitted synchrotron power, so that their ratio reduces to:

$$\frac{P_{synch}(r)}{P_{compt}(r)} = \frac{U_B(r)}{U_{ph}(r)}$$

In this context, synchrotron and inverse Compton radiation can be distinguished by their dependence on a single parameter. Thereby it is possible for either component to significantly dominate over the other, in either the case of an electron population with a much larger surrounding magnetic field, or the case of an electron population with a much larger photon density. However, while it is possible to have an electron population in the absence of magnetic fields emit only in-

# The Spatial Extension of the Inverse Compton Component of the Crab Nebula

## 2 The Crab

---

verse Compton radiation, the reverse is not possible. Since synchrotron emission produces photons, it will inadvertently produce a local photon density, which also produces inverse Compton radiation. Thus, any synchrotron source will reappear at its initial size in a higher energy range as an inverse Compton source, within the background of additional inverse Compton sources.

For the Crab nebula, this means that measuring the extension of its inverse Compton component should yield at least the size of its synchrotron component. The inverse Compton Crab nebula may also be larger, which would hint at the existence of otherwise cold electron populations with no magnetic field within the nebula. It could appear smaller due to the measured inverse Compton component being the boosted emissions of the X-ray synchrotron nebula, which is smaller. In this case, the electron populations' average Lorentz factor are relatively small, and the inverse Compton component from the radio nebula would appear at smaller energies which are harder to locate through the background of emissions from the synchrotron nebula as well as the pulsar. In either case, the inverse Compton component delivers vital information on the exact composition of the nebula.

## 2.4 Markarian 421:

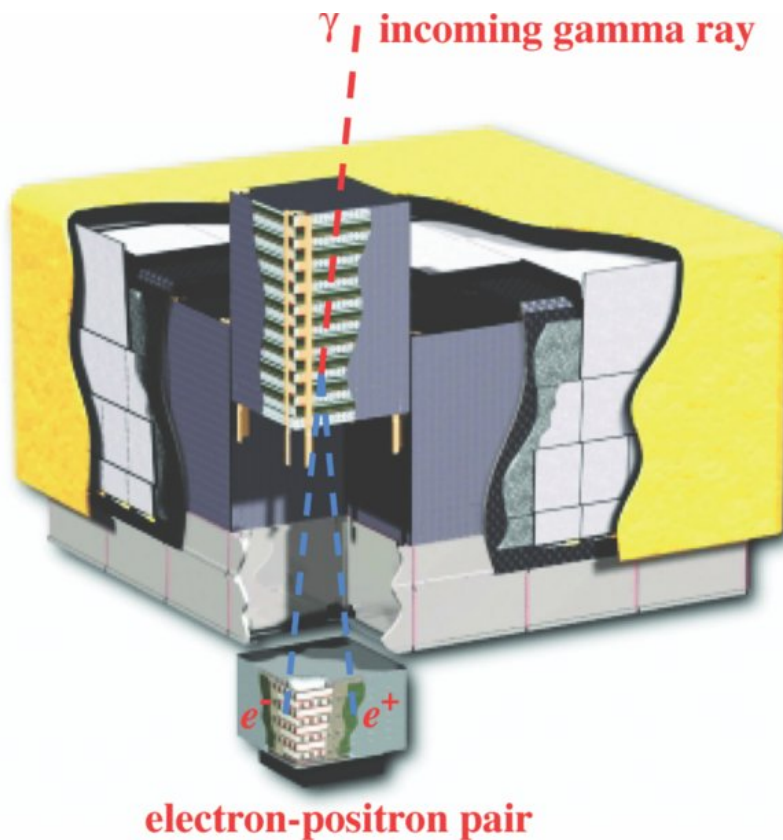
Markarian 421 (Mkn 421) is a blazar located at right ascension  $11^{\text{h}} 04^{\text{m}} 27.31^{\text{s}}$ , declination  $38^{\circ} 12' 31.8''$ , and a redshift of  $z = 0.031$  and is one of the brightest extragalactic gamma-ray sources in the sky (Abdo et al. 2011). It is a source with major outbursts consisting of many short flares about once every two years (Bartoli et al. 2015).

Blazars are galaxies with strong emission from the accretion of mass by a supermassive black hole at their center (so called Active Galactic Nuclei). They have two highly collimated, relativistic jets coming out the accretion disk from opposite sides, which are seen from earth at a small

# The Spatial Extension of the Inverse Compton Component of the Crab Nebula

## 2 The Crab

---



angle. They are very variable regarding their emissions over extended periods of time. Blazars are the dominant source of radiation in the extragalactic very-high-energy sky (energies  $> 0.1$  TeV) (Bartoli et al. 2015).

The flux and also the spectrum of Markarian 421 are highly variable. During a 4.5-year multi-wavelength observation, Bartoli et al. (2015) observed seven flares, ranging in duration from a few days to a few weeks, falling into three categories within the Fermi LAT energy regime: those with little variation in spectrum and flux, those with high variation in flux only, and those with a hardening of the spectrum only. The flux varied by a factor of up to 12, while the spectrum varied up to 0.27 in difference of spectral indices during some of these flares.

For this thesis, Markarian 421 was chosen as a pointlike reference source, on which the analysis procedure could be repeated. It was chosen since it is an extragalactic source with a flux comparable to that of the Crab nebula at very-high energies. The high variability of its flux is not

# **The Spatial Extension of the Inverse Compton Component of the Crab Nebula**

## *2 The Crab*

---

expected to cause any problems during the analysis.

## 3 Fermi LAT

This chapter follows the detailed description of the Fermi LAT experiment found in Atwood et al. (2009).

The Fermi Large Area Telescope (Fermi LAT) is a high-energy gamma-ray telescope based on the Fermi Gamma Ray Space Telescope (Fermi) mission, with an energy coverage ranging from 20 MeV up to more than 500 GeV. It started data taking on August 4<sup>th</sup> 2008, shortly after the launch of the Fermi Satellite on June 11<sup>th</sup> 2008. Similar to its predecessor, the Energetic Gamma-Ray Experiment Telescope (EGRET), it is designed to survey the entire sky. Its basic layout can be seen in figure 3.1.

Its primary mission objectives are (Atwood et al. 2009, p.3) “(1) determining the nature of unidentified sources and the origins of the diffuse emissions revealed by EGRET, (2) understanding the mechanisms of particle acceleration operating in celestial sources, particularly in active galactic nuclei (AGNs), pulsars, supernovae remnants, and the Sun, (3) understanding the high-energy behavior of GRBs [Gamma Ray Bursts] and transients, (4) using gamma-ray observations as a probe of dark matter, and (5) using high-energy gamma-rays to probe the early universe and the cosmic evolution of high-energy sources to [redshifts]  $z \geq 6$ .”

As a satellite-based telescope, Fermi LAT has some advantages and some disadvantages over ground-based telescopes. Its main advantage is to be able to detect the incident photon right at its interaction point, as the initial photon interaction takes place inside the detector. Ground-based experiments can only measure particles on ground-level, after they have started a particle cascade within the earth's atmosphere. In theory, this should lead to a much superior resolution in energy, direction and identification of incoming particles for satellite-based experiments, although in practice, ground-based experiments have found sophisticated analyses to reach similar resolutions and identification through the use of multiple detector types and the measurement of additional

## The Spatial Extension of the Inverse Compton Component of the Crab Nebula

### 3 Fermi LAT

---



**Figure 3.1:** Highlighted is one of the 16 identical modules that make up Fermi LAT. Incoming gamma-rays convert into an electron-positron pair in the tracker (top). This electron pair is then tracked before its energy is measured in the calorimeter (bottom). The Anti-Coincidence Detector which surrounds the structure can be seen to the side. (Atwood et al. 2009)

parameters, such as direct Cherenkov light deposition or muon count (Aharonian et al., 2007; PAC 2015). Its main disadvantage is its limited size due to the limited size of the host satellite. While modern ground-based detectors cover square kilometers of effective target area, satellite-based detectors are limited to sizes less than a square meter. As the particle flux quickly drops off with energy, satellite-based detectors can only cover smaller energy ranges (MeV to GeV scale) to maintain the same event rates, which does complement the ground-based telescopes, as these energies are not entirely covered by them (GeV to TeV scale).

This chapter will deliver a detailed account on the makeup and workings of Fermi LAT. The first part goes over each of its individual components. The second part gives a summary of the total event reconstruction and subsequent acceptance/rejection. The third part will explain the

# The Spatial Extension of the Inverse Compton Component of the Crab Nebula

## 3 Fermi LAT

---

Fermi tools, software provided by the Fermi Science Support Center (FSSC) to analyze Fermi LAT data.

### 3.1 Fermi LAT Components:

At the energy range covered by Fermi LAT, gamma-rays mainly interact with matter via the production of electron-positron pairs. The cross section of this process is highly dependent on the electron density of the target material, meaning substances with a high atomic number  $Z$  are preferred. The produced electron-positron pair can then be tracked and its properties measured to infer the properties of the initial photon. Thus, the detection of high energy gamma-rays is a two part process: first is the conversion of the gamma-ray into an electron-positron pair within suitable converter material, followed by measurements on the electron-positron pair in the following detector parts.

Fermi LAT consists of detector technologies with “an extensive history of application in space science and high-energy physics with demonstrated high reliability” (Atwood et al. 2009, p.4), with its systems and subsystems being tested in accelerator beams. Its main features are a precision converter-tracker (section 3.1.1), a calorimeter (3.1.2) supported by a low-mass aluminum grid structure, a segmented anti-coincidence detector (ACD), as well as a programmable trigger and data acquisition system (DAQ, 3.1.3), all arranged into 16 identical modules in a four-by-four grid. These parts will be discussed in the following subsections. The aspect ratio of its height to width is 0.4, to maximize its field of view, while also ensuring that as many pair-conversion events as possible pass into the calorimeter after triggering. Fermi LAT is able to self-trigger, thanks to the silicon strip detectors it uses not requiring an external trigger. The DAQ uses onboard processing to reduce the rate of events transmitted to a manageable 1 Mbps by focusing on the rejection of cosmic ray events. None of its components use any consumables such as gas.

# The Spatial Extension of the Inverse Compton Component of the Crab Nebula

## 3 Fermi LAT

---

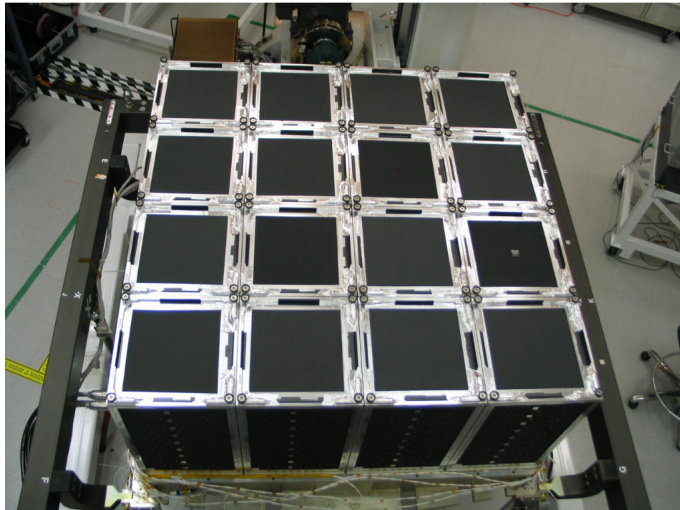


**Figure 3.2:** The whole 4-by-4 array of converter-tracker modules before integration with the ACD. (Atwood et al. 2009)

### 3.1.1 Precision Converter-Tracker:

Each converter-tracker module (figure 3.2 and 3.3) consists of 18 tracking planes, each made up of two layers of single-sided silicon strip detectors (SSDs). Strips of the same layer are parallel, while those of the proximate layer are rotated by 90 degrees, to allow for proper resolution in both x- and y-direction. The first 16 planes also contain a layer of high-Z tungsten for conversion on top. So, each conversion layer is followed by at least three double-layers of SSDs (see figure 3.4).

One of the most important features of the Fermi LAT tracker is its division into two regions. The first twelve layers make up the “front” region. Here the converter foil of each layer is relatively thin (0.03 radiation lengths), allowing for an immediate, and thereby more precise, tracking of the electron-positron pair after conversion and an improvement of the point-spread function.

**Figure 3.3:** One of the 16 converter-tracker modules opened at one side. (Atwood et al. 2009)

## The Spatial Extension of the Inverse Compton Component of the Crab Nebula

### *3 Fermi LAT*

---

The remaining six layers make up the “back” region, containing four much thicker converter foils (0.18 radiation lengths). This allows for a significant increase in effective area available for detection. The general idea is to first attempt to track each incoming photon with the maximum obtainable precision, then try to catch as many of the photons having slipped through the front region, with less of a regard towards precise tracking. The front and back regions are balanced in such a way that they have roughly the same sensitivity to a LAT point source, although the exact ratio is dependent on each source's specific spectral characteristics.

The silicon strip detectors are 8.95 cm x 8.95 cm x 400  $\mu\text{m}$  in size, with aluminum readout strips spaced at distances of 228  $\mu\text{m}$ . Sets of four SSDs are bonded into “ladders” of about 35 cm length, with four of these ladders mounted next to one another at 0.2 mm distance. The SSDs contain dead area of roughly 1 mm length off to their sides. The tungsten converter foils only cover the active part of the SSDs.

The ability to track an incident photon is measured in terms of the point-spread function (PSF). This function describes how the reconstruction of photons originating from a single point source are distributed and is usually denominated by its 68% containment radius. The PSF is mostly limited by the multiple scattering of and production of bremsstrahlung by the electrons. As these effects get less distorting with increasing energy, the PSF improves. This makes the PSF strongly dependent on energy.

# The Spatial Extension of the Inverse Compton Component of the Crab Nebula

3 Fermi LAT

---

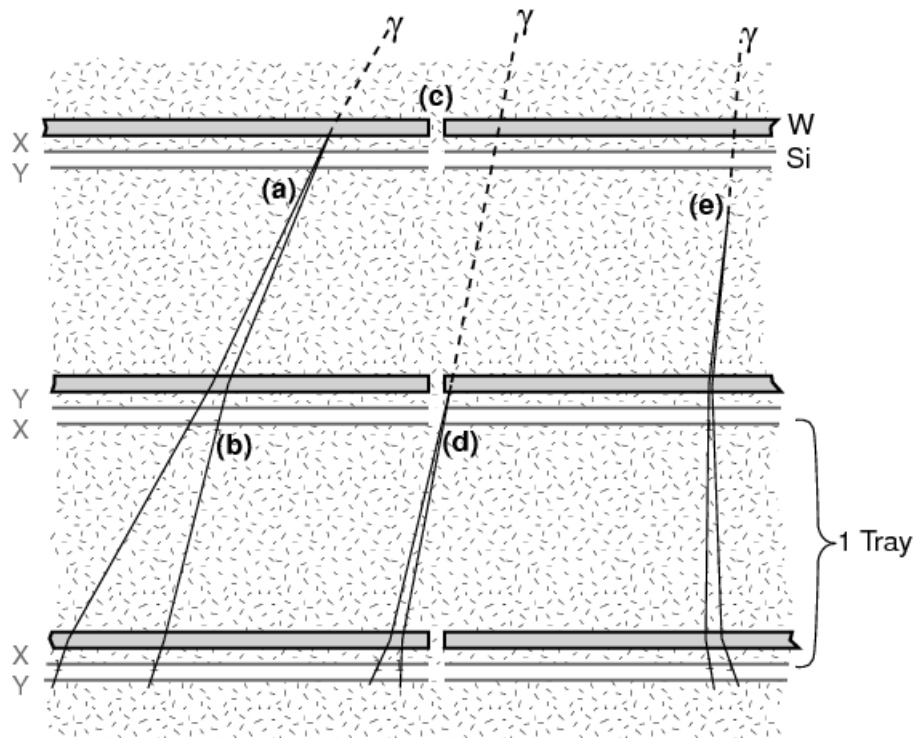


**Figure 3.4:** Illustration of the Fermi Converter-Tracker design principle. Photons are first converted into charged particles in the W converter foil (gray) and then tracked in the Si detectors (white). The additional y-axis tracking is not portrayed. The illustration shows an ideal photon conversion and tracking (a), as well as suboptimal tracking due to a missed hit (d) and conversion within structural elements (e). The latter cases significantly decrease the resolution. (Atwood et al. 2009)

Triggering is achieved through measuring a coincidence in successive layers. Additionally, the time-over-threshold for each readout is kept and later used for background rejection. The rest of the tracker design is for the most part focused on minimizing dead area and maximizing sustainability. For example, each plane is embedded into a tray made of carbon, chosen primarily for its small weight and long radiation length. Also, each tracker layer has two readout electronics, which are placed at the side, as not to interfere with the tracking.

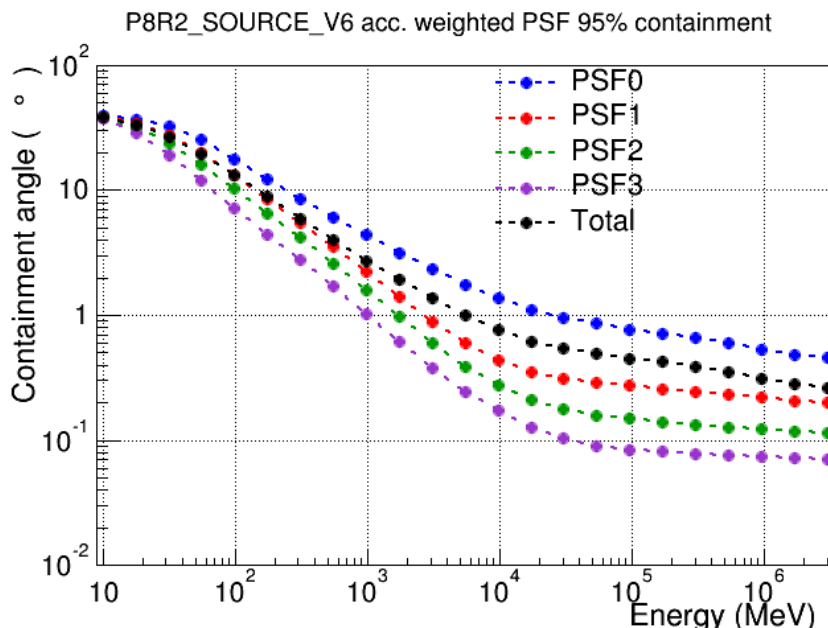
# The Spatial Extension of the Inverse Compton Component of the Crab Nebula

## 3 Fermi LAT

### 3.1.2 Calorimeter:

Each calorimeter module consists of 96 CsI crystals of size 32.0 cm x 2.7 cm x 2.0 cm, arranged in eight layers of twelve crystals. Its depth of 2.0 cm corresponds to a total length of 8.6 radiation lengths (10.1 when including the tracker) for the entire setup. Neighboring modules are rotated by 90 degrees for segmentation in x- and y-direction to form a hodoscopic array (Carlson et al. 1996). All crystals are optically isolated from one another.

Each crystal has four PIN-photodiodes as readouts, two on either side of its long dimension. They measure the scintillation light transmitted to their respective ends. The layout of the diodes allows for a more precise measurement of the shower position, based on light asymmetry. Alongside the position of the crystal within the module, this means the shower can be reconstructed in all three spacial dimensions. The photodiode pairs consist of a large diode (area of 147 mm<sup>2</sup>),



covering an energy range from 2 MeV to 1.6 GeV and a small diode (area of 25 mm<sup>2</sup>) covering 100 MeV to 70 GeV.

The longitudinal segmentation allows for measurements up to TeV energies. These energies are reached through the readout of multiple crystals (catching the electron and the positron) and through estimates of shower leakage. The energy resolution is only limited by the statistical fluc-

# The Spatial Extension of the Inverse Compton Component of the Crab Nebula

## 3 Fermi LAT

---

tuation of shower leakage.

### 3.1.3 Trigger and Anti-Coincidence Detector:

The Fermi LAT Data Acquisition System (DAQ) works hierarchically. At the lowest level, there are 16 Tower Electronics Modules (TEMs), one for each detector module, directly connected to the tracker and calorimeter pair. These can initiate a trigger request by two means: (1) if a tracker channel is over threshold and additional criteria, such as hits in three successive planes, are met, or (2) if any of the calorimeter crystals exceeds a certain energy threshold. In either case the trigger request is sent to the Global-trigger Electronics Module (GEM). This request is complemented with input from the Anti-coincidence detector (ACD).

The ACD consists of plastic scintillators covering the outside of the module array. These scintillators detect incoming charged particles based on the signal they leave inside, a signal that is not left by charge-neutral photons. This signal is used for the rejection of charged particle background. The plastic scintillators are made up of tiles (segmented parts), with the light collected by wavelength-shifting fibers. The ACD achieves a 99.97% detection efficiency of charged particles, meeting the requirement to reduce the background to rates below those of gamma-ray acceptance.

A challenge of the ACD is the so-called backplash effect. Secondary photons produced within the calorimeter shower may Compton scatter in the ACD and create false vetoes. To avoid this, the ACD is segmented and only the segment near the incident photon track is considered. At high-energy events (above  $\sim 20$  GeV) the trigger ignores the ACD and the data is recorded in all cases to get analyzed using more complex software on Earth.

If the trigger request meets the criteria posed by the GEM, a trigger accept message is sent to each TEM and ACD module, responded to by a trigger acknowledgment signal. This causes the entire instrument to be read out.

The signal is then sent to the instrument-level event builder module (EBM), which passes it on

# The Spatial Extension of the Inverse Compton Component of the Crab Nebula

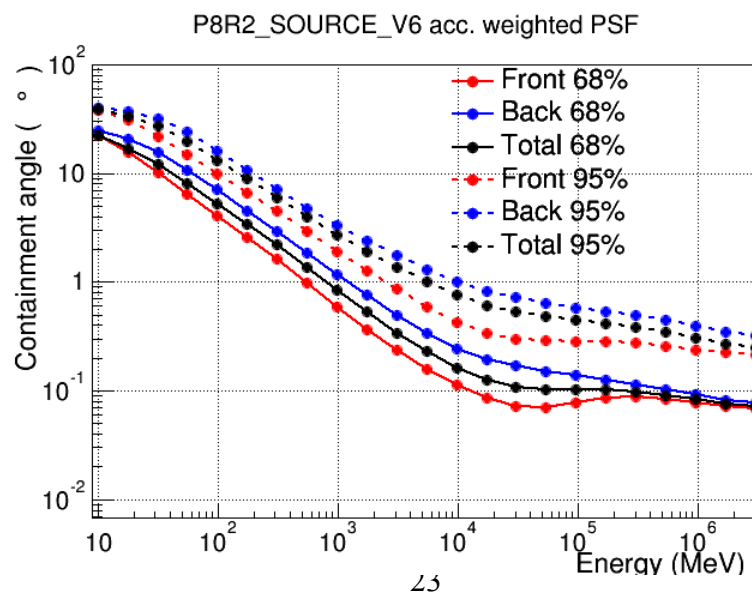
## 3 Fermi LAT

---

to the Event Processor Units (EPUs). There are two EPUs on board, applying filter algorithms to reduce the event rate from 2-4 kHz down to 400 Hz which can then be downlinked to and further processed on earth. The filter algorithms are largely focused on rejecting charged particle events while also maximizing the number of gamma-ray kept within the manageable rate.

### 3.2 Data Format:

All Fermi data is publicly available from the FSSC (2016) website. Fermi data consists of two types of files. The first type is the event file, in which all information about the reconstructed photons, such as energy and position, is stored. The second type is the spacecraft file which stores all positional and timing information about the Fermi satellite. The latter is mostly used to determine Fermi's momentary field of view or calculate barycentric corrections, while analysis work is mostly done on the former.



## The Spatial Extension of the Inverse Compton Component of the Crab Nebula

*3 Fermi LAT*

---

**Figure 3.5:** The 68% and 95% containment radii of the PSF for front- and back-converted events. Front-converted events have an improved PSF of a factor of 2, due to the proximity of converter foil and tracker. (SLAC 2016)

# The Spatial Extension of the Inverse Compton Component of the Crab Nebula

## 3 Fermi LAT

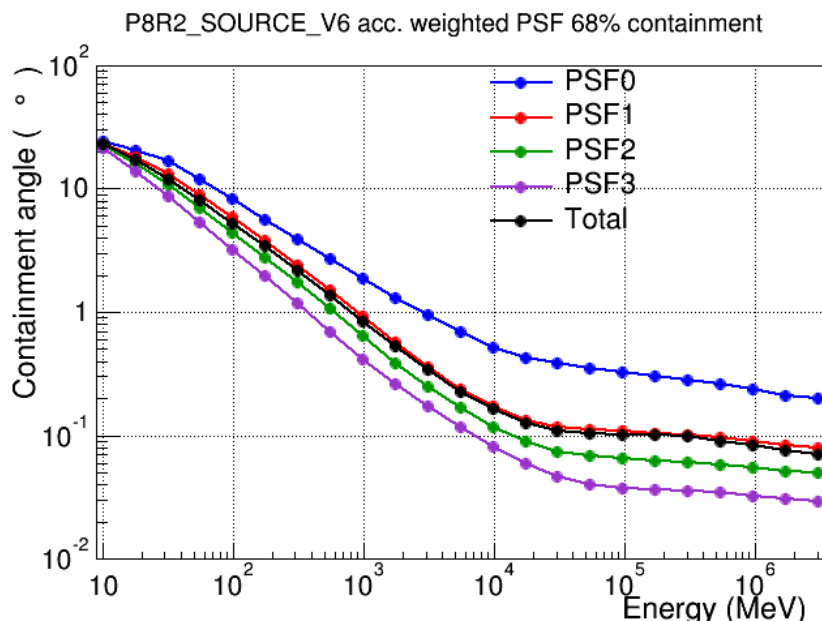


**Figure 3.6 & 3.7:** The 68% and 95% containment radii of the PSF for the different PSF classes. Each PSF corresponds to 25% of event data. Through this partition, the PSF can be improved by a factor of 10 between poor PSF events (PSF0 class) and good PSF events (PSF3 class). (SLAC 2016)

The reconstruction of Fermi data has, over time, undergone a few changes. The current iteration of data reconstruction (so called Passes) is Pass 8, which offers a number of improvements over the previous Pass 7 installment. Most important for this Master's thesis is the extension of the photon event classes. Previously, the data was only partitioned into front-converted and back-converted events (see figure 3.5), each with its own set of Instrument Response Functions (IRFs). With Pass 8, the data is additionally partitioned into quartiles by PSF and energy dispersion, with each partition having its own IRFs that can not be mixed. The division of the data into these quartiles has been confidently determined over time and is based on information from all Fermi LAT detector parts, such as the total number of tracker hits and the number of additional tracks within the tracker. Figures 3.6 and 3.7 show the difference in PSF between each PSF type. For more information on Pass 8 see Atwood et al. (2016) or SLAC (2016).

### **3.3 Fermi Tools:**

A number of computer programs to evaluate Fermi LAT data, called Fermi tools, are readily made available at the Fermi Science Support Center (FSSC 2016). The purpose of these programs ranges from simple cuts on data over likelihood analyses to full simulations of event and spacecraft data. The programs frequently used over the course of this Master's thesis are explained below.

*gtselect:*

gtselect is used to apply additional cuts on data in order to create smaller subsamples. The cuts are mostly the same as those already applied upon data selection, such as cuts on energy, time, or event class. One additional cut is that on the maximum apparent zenith angle, advised to be 90 degrees. These cuts are then compatible with the usage of other Fermi tools.

*gtmktime:*

gtmktime is used to make cuts on data based on the spacecraft file. It uses information from the spacecraft file to create so-called “good time intervals”, based on satellite orientation and the earth's position to ensure that the data is valid, especially checking if the source was, at the moment of data taking, not too close to the earth's limb.

*gtpphase:*

gtpphase is used to calculate the pulse phase of incoming photons. It uses the pulsar's ephemeris information, fed to the program separately, then applies barycentric corrections to calculate the arrival times from the pulsar's frame of reference.

*gtobssim:*

gtobssim is used to simulate data sets based on source input and spacecraft files. It is able to

## **The Spatial Extension of the Inverse Compton Component of the Crab Nebula**

*3 Fermi LAT*

---

handle point as well as extended or even isotropic sources. It works by generating photon events based on the sources spectral information, then randomly applies errors to the photon reconstruction based on the instrument response functions. Note that the instrument response functions for these simulations are simplified compared to real data. It is only possible to simulate singular IRFs, i.e. those for front-converted events only or for PSF3 events only. “Real” simulations are therefore generated through the stacking of multiple gtobssim simulations.

# 4 Data Selection

## 4.1 Initial Data Set:

The analyzed data set was downloaded from the FSSC website (see section 3.2) using the following input parameters:

- Object name or coordinates: Crab (RA = 83.6331°, DEC = 22.0145°)
- Coordinate system : J2000
- Search radius (degrees): 15
- Observation dates: START (2008-08-04 15:43:36 ), 2015-06-30 23:59:59
- Energy range: 1000, 2000000

The data covers a time span of almost seven years, from August 2008 to June 2015. A second identical data set was created by cutting the first (hereafter referred to as full time data) into pieces covering a time span of one month each (hereafter referred to as piecewise data). All pieces cover exactly one month starting from the 1<sup>st</sup> day of the month to the last with the exception of September 2011 and November 2011, which were further cut into two and three parts respectively to account for rapid changes of the pulsar phase during these times. The piecewise data allows for an easier handling of the Crab pulsar ephemeris, as it is also defined individually over the same 1-month time periods (including September 2011 and November 2011). The energy range was chosen to begin at a point where the nebula's inverse Compton component significantly dominates over its synchrotron component (1000 MeV), and end at the highest energies detectable by Fermi LAT (> 1000000 MeV). The search radius of 15 degree is a standard value for Fermi LAT searches. It is designed to locate any other sources whose radiation may partially be reconstructed in proximity to the Crab nebula. It has to account for both the Crab nebula's as well

# The Spatial Extension of the Inverse Compton Component of the Crab Nebula

## 4 Data Selection

---

as the other source's PSF. Since the PSF improves with energy (see figure 3.6), and the radius of 15 degrees was chosen for the worst PSF at 30 MeV, this radius could have been made smaller, but was kept the same out of convenience.

In this case, the word radius refers to the angular separation on the celestial sphere and is therefore calculated differently from the radius on a flat plane. The haversine formula is used to calculate the angular separation between two points  $(RA_1, DEC_1)$  and  $(RA_2, DEC_2)$  as:

$$r = \sin^{-1}(\sqrt{\sin(\Delta DEC)^2 + \cos(DEC_1)\cos(DEC_2)\sin(\Delta RA)^2})$$

One additional cut was applied through the Fermi tools `gtselect` and `gtmktime` in their standard settings. This cut requires the remaining photon data to have a maximum apparent zenith angle of  $90^\circ$ . It is made as to not include any secondary photons created by cosmic rays within the earth's atmosphere.

To account for the remaining background from the Crab pulsar, all photons were assigned a pulsar phase through the use of the `gtpphase` Fermi tool and proper ephemeris data. As per norm, this pulsar phase ranges from 0.0 to 1.0, with 0.0 corresponding to the main peak of the current and 1.0 to the main peak of the next pulse. For this analysis, ephemeris data was taken from the Jodrell Science Bank of Astrophysics (Lyne, Pritchard & Graham-Smith 1993). As the ephemeris are defined for individual months, the pulsar phase was only assigned to the piecewise data. Some days were not covered by the ephemeris and subsequently cut.

`gtpphase` was unable to evaluate the proper times of arrival and recreate the main peak at the pulsar phase value 0.0. Instead, the main peak was located at a random phase for each month. The location of the main peak was shifted to 0.0 manually. For this, the pulsar phase was divided into 100 bins, each corresponding to 0.01 pulsar phase. Then the bin with the maximum number of entries was assigned the value 0.0. A veto required the secondary peak (as a local maximum) to be located at 0.3 - 0.5, roughly corresponding to the expected peak position at 0.4 (see figure 2.2). Otherwise, the main peak value would be reassigned to the secondary peak value and the requirement checked again. The veto did not trigger for any of the monthly data, meaning that the main peak was exclusively stronger than the secondary peak. The full data phasogram can be seen in

## The Spatial Extension of the Inverse Compton Component of the Crab Nebula

### *4 Data Selection*

---

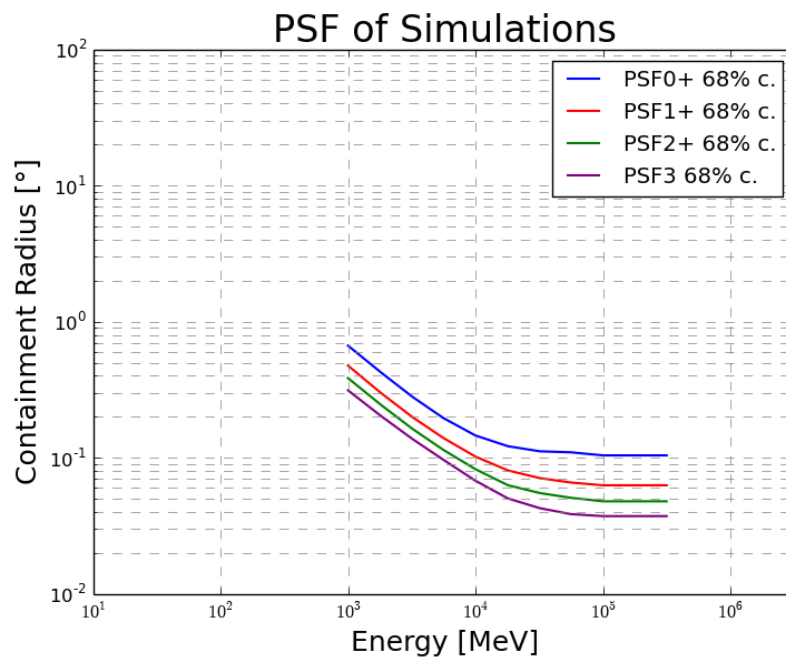
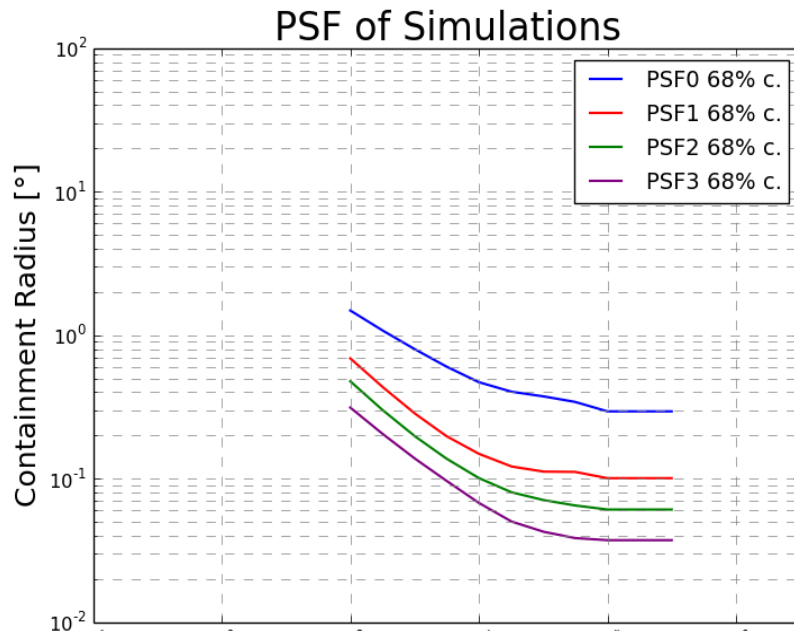
figure 4.1.

The off-pulse phase was estimated to be at  $0.49 < \phi < 0.89$ . A cut was made on the piecewise data to keep only the off-pulse data. This cut eliminates all pulsar photons, keeping only photons stemming from the Crab nebula (synchrotron and inverse Compton) and other background sources. This cut also reduces the number of nebula events by the relative size of the off-pulse window to the full pulsar phase, which is a factor of 0.4.

# The Spatial Extension of the Inverse Compton Component of the Crab Nebula

## 4 Data Selection

---



**The Spatial Extension of the Inverse Compton Component of the Crab Nebula**  
*4 Data Selection*

---

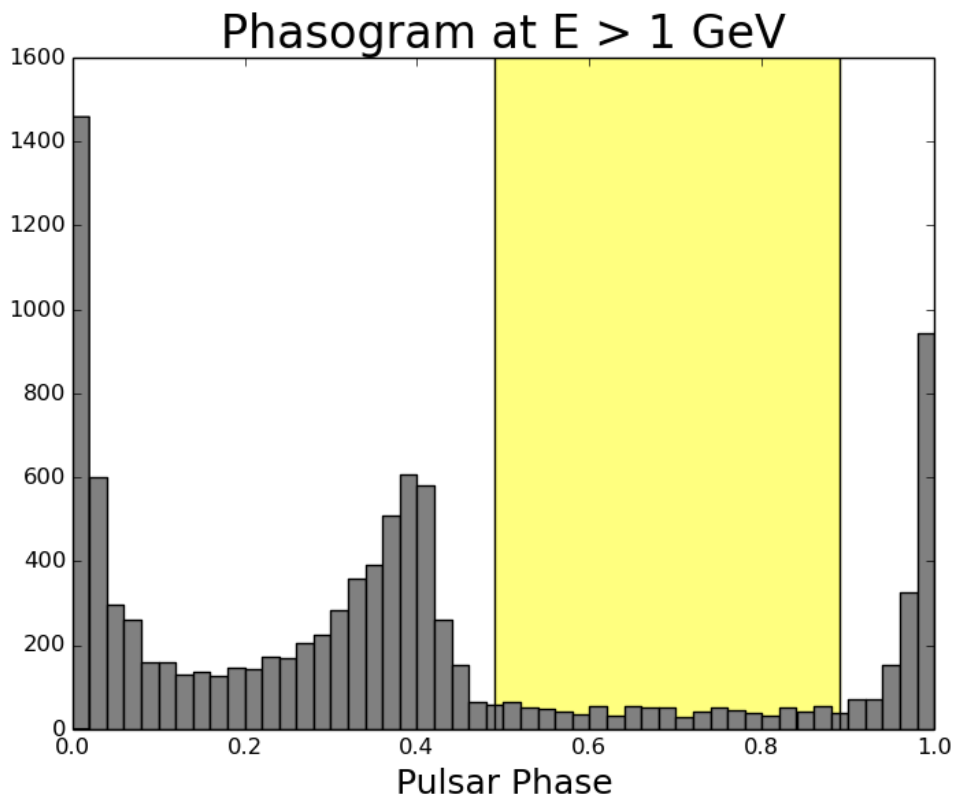


**Figure 4.1:** A phasogram of the whole Crab data set. The energy range covered is 1 – 2000 GeV. The bin size is 0.02 of the pulsar phase. The data shows the typical Crab pulsar profile (compare to figure 2.2) with the main pulse located at 0.0 and the secondary pulse located at 0.4. The off-pulse region was determined to be between 0.49 and 0.89 (yellow).

## 4.2 Simulations:

A number of models were created to describe the Crab nebula in its spatial extension. All models assume a “tophat” profile for the Crab nebula, in which the flux is homogeneous inside a certain radius  $r$  around the center and drops off to 0 at the edges. The radii for these tophat models ranged from a pointlike source in steps of  $0.05^\circ$  to a maximum of  $0.10^\circ$  for a total of 21 models. As the radio Crab nebula is elliptical in shape, these models are not expected to recreate the Crab data fully, but instead give a general idea of its average extension.

A data set was simulated for each nebula model using the Fermi tool `gtobssim`. The simulated

# The Spatial Extension of the Inverse Compton Component of the Crab Nebula

## 4 Data Selection

---

spectrum was the same for each model. This spectrum was an amplified version of the inverse Compton Crab nebula spectrum taken from Bühler (2011) with the amplification factor 100 to increase the amount of test statistics. They were done in both a piecewise and a full time fashion. In the same fashion, models for Markarian 421 were created, using the same spatial templates, but a different spectrum and a smaller amplification factor of 10. The spectrum for Markarian 421 was taken from the Fermi LAT 4-year catalogue (FERMI 2016), which has compiled information on all sources Fermi LAT has identified in the first 4 years of its running.

Additional background simulations were created. For this, the Fermi LAT 4-year catalogue was browsed for all sources within a 15 degree radius around the Crab pulsar. These sources were then collectively simulated in one background file using the listed spectra and, if existent, spatial extensions. All sources with no listed spatial extension were assumed to be pointlike. Additionally, the galactic background and the isotropic background were simulated in the same file, using the models provided at FERMI (2016). The total flux of the galactic and isotropic background were calculated through integration of the provided spectra and spatial maps. The only sources excluded from the background simulation were the three Crab sources: the Crab pulsar, the synchrotron Crab nebula, and the inverse Compton Crab nebula. A background simulation for Mkn 421 was done the same way, except with only sources in a 5 degree radius around Mkn 421 included (save for Mkn 421 itself).

As `gtobssim` can only handle one set of IRFs at a time, the simulations were done individually for each PSF class. Additional simulations for exclusively front- or back-converted data were considered, but decided against. Cuts on the conversion type could help further improve the PSF, as front-converted events have a much better PSF than back-converted events, but conversion types and PSF types are correlated enough to make such an additional cut needless (see figure 4.2). Therefore, the data was simulated as the different PSF types only, and the full model is reconstructed by adding up some or all of these four PSF simulations.

All simulated energy spectra drop off at 500 GeV due to simulation limitations. The effect of this cutoff is manageable, since at this energy range the PSF function has already reached a plat-

## **The Spatial Extension of the Inverse Compton Component of the Crab Nebula**

### *4 Data Selection*

---

teau and the Crab only records about two dozen events above these energies, which behave like 500 GeV events. These events can reliably be compensated by reweighting lower energy simulations to compensate.

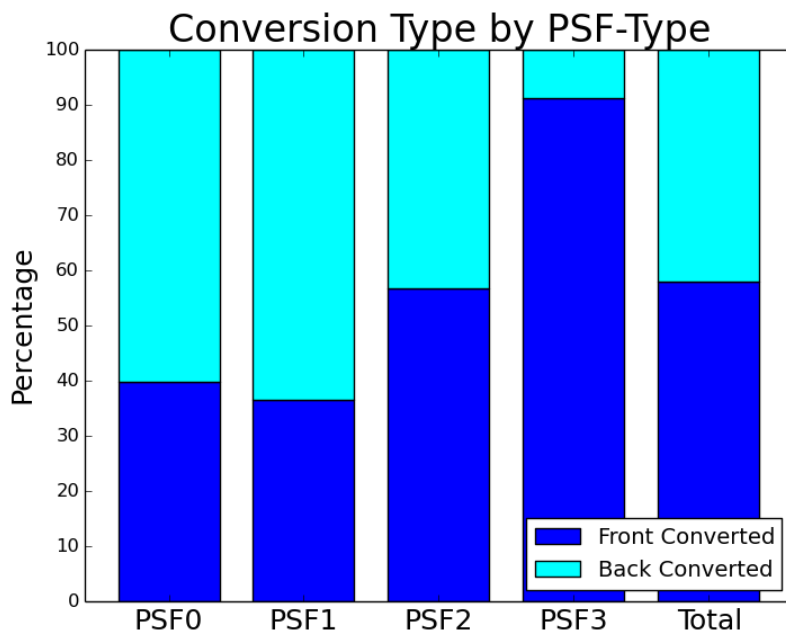


**Figure 4.2:** The composition of conversion types for the different PSF types in the full time data set. Less than 10% of events in the highest PSF quartile are back-converted, implying a correlation between these two partitions.

### 4.3 Applied Cuts:

In addition to the cut on the pulsar phase, three other cuts were considered to increase the obtainable resolution of the data set. These were cuts on angular separation, energy, and PSF class.

#### *Angular separation cut:*

The initial search radius of 15 degrees still contains a large portion of the sky, including many background sources. For a proper source analysis, it is necessary to eliminate as many of these background sources as possible. Since most of these sources are far away from the Crab, this can be most easily achieved by a cut on the angular separation between the photons and the Crab pulsar. The exact cut value needs to be as small as possible to eliminate as many background sources as possible, while still being large enough to contain most of the data and simulation nebula photons, to make a distinction between the different model templates possible. The latter is

# The Spatial Extension of the Inverse Compton Component of the Crab Nebula

## 4 Data Selection

---

the case, if the cut value is several times larger than the PSF. Only two cut values were considered:  $0.5^\circ$  in the case of a low energy cut, and  $0.25^\circ$  in case of a high energy cut. Figure 4.3 showcases the percentage of simulated photons contained in a  $0.25^\circ$  radius around the center after the final cuts were applied. This percentage does not drop off significantly up to the largest model, meaning this angular separation cut fulfills the demanded requirement.

### *Energy:*

A cut on energy has several effects on the data set. First, it reduces the number of signal Crab nebula events. At the same time, it also reduces the number of background events. The ratio of signal to background improves with increasing energy, as the inverse Compton nebula has a harder spectrum than all considered background sources. Also, the PSF improves considerably with increasing energy. An optimal cut would balance these three effects.

Nine energy cuts in total were considered on energies in roughly logarithmic steps of 0.25 from  $10^3$  to  $10^5$ .

Figures 4.4 and 4.5 show the energy dependence of the PSF for each PSF class individually and for every PSF class stacked with higher PSF classes for the pointlike model simulation.

# The Spatial Extension of the Inverse Compton Component of the Crab Nebula

## 4 Data Selection

---

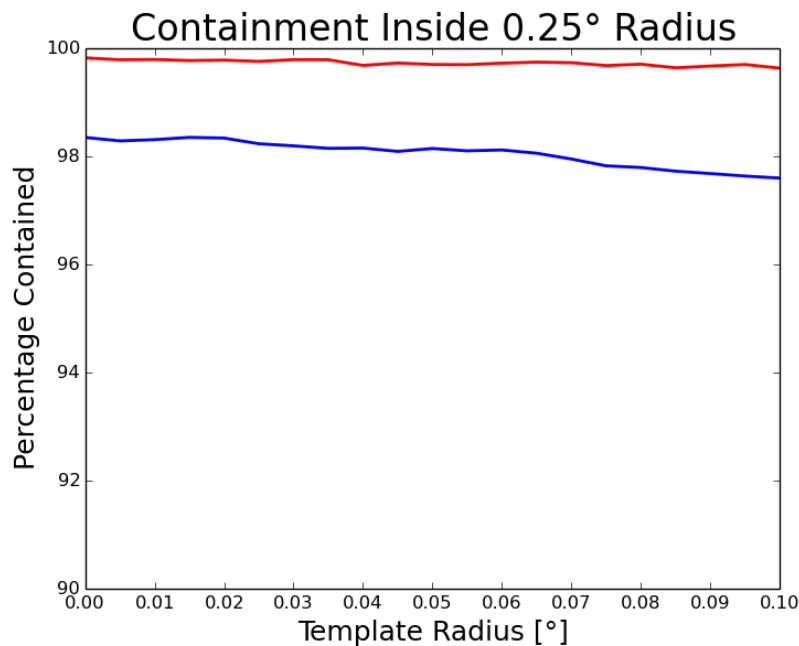


**Figure 4.3:** The amount of simulated photons contained in a  $0.25^\circ$  radius around the center for all spatial models after the final cuts were applied. The red line represents PSF3 data, the blue line PSF2 data. In both cases, more than 97% of the photons are contained inside this radius, independent of the template used.

### *PSF Class:*

A cut on the PSF class has a similar effect as a cut on energy. It also improves PSF and reduces both signal and background, although it does leave the signal to background ratio largely untouched. Again, an optimal cut will compromise between the improvement of PSF on the one side and the reduction of signal on the other. The PSF cuts considered were on any number of the lowest PSF classes. This results in four possible cuts from cutting no PSF classes to cutting the PSF classes 0 to 2 from the data.

**Figure 4.4 & 4.5:** The 68% containment radii for the different PSF types as a function of Energy as determined from the simulation of the pointlike model template. At the top are the PSFs for each PSF class individually. At the bottom are the total PSFs of each PSF class stacked with higher PSF classes. PSF0+ corresponds to the total PSF. The PSFs are in accordance with the

# The Spatial Extension of the Inverse Compton Component of the Crab Nebula

## 4 Data Selection

---

model PSFs (figure 3.6)

Figures 4.6 and 4.7 show the energy dependence of Crab data and simulated background for the different PSF classes in a  $0.25^\circ$  radius around the Crab pulsar. The exact PSF composition shows an interesting behavior for the data. At first higher PSF classes dominate. This is due to the PSF of lower classes being too large to fit entirely inside the cut radius. At medium energies, the composition becomes more equalized, as all PSFs improve to a level which fits inside the radius (although the PSF0 class does not achieve values lower than  $0.25^\circ$ ). At higher energies, the exact composition is dominated by statistical error, although here lower PSF classes may start to dominate. At higher energies, events are more likely to deploy multiple tracker and calorimeter hits, which makes reconstruction much more uncertain. Events with too much uncertainty then cannot fulfill the strict PSF2 or PSF3 requirements.

To find the cuts to gain the best obtainable resolution, this best obtainable resolution needs to be quantified. For this thesis, the obtainable resolution will be quantified as the total error on the position of the center of a data set in right ascension and declination. This error can be estimated from the data as follows:

For a single signal photon, the error on the data center is given by the error on this photon's position. This error is proportional to the point spread function, since right ascension and declination are only correlated by a scaling factor. As it does not contribute to the relative precision, the proportionality factor is set to one for simplicity:

$$\sigma_{Total}^2(N_{signal}=1) = \sigma_{PSF}^2$$

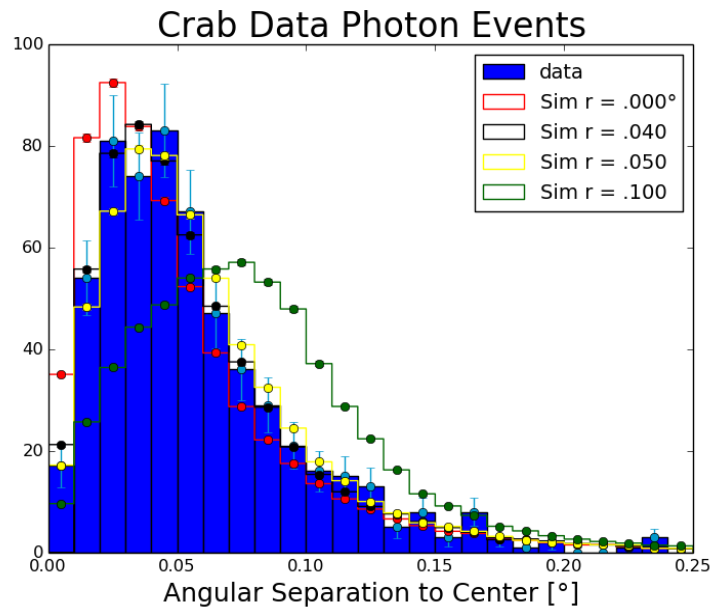
For  $n$  signal photons, the center location becomes the mean value of all photons, and their errors add quadratically. As their errors are assumed to be the same, this simplifies to:

$$\sigma_{Total}^2(N_{signal}) = \sum_{i=1}^{N_{signal}} \left( \frac{\sigma_{PSF}}{N_{signal}} \right)^2 = N_{signal} \frac{\sigma_{PSF}^2}{N_{signal}^2}$$

# The Spatial Extension of the Inverse Compton Component of the Crab Nebula

## 4 Data Selection

---



# The Spatial Extension of the Inverse Compton Component of the Crab Nebula

## 4 Data Selection

---

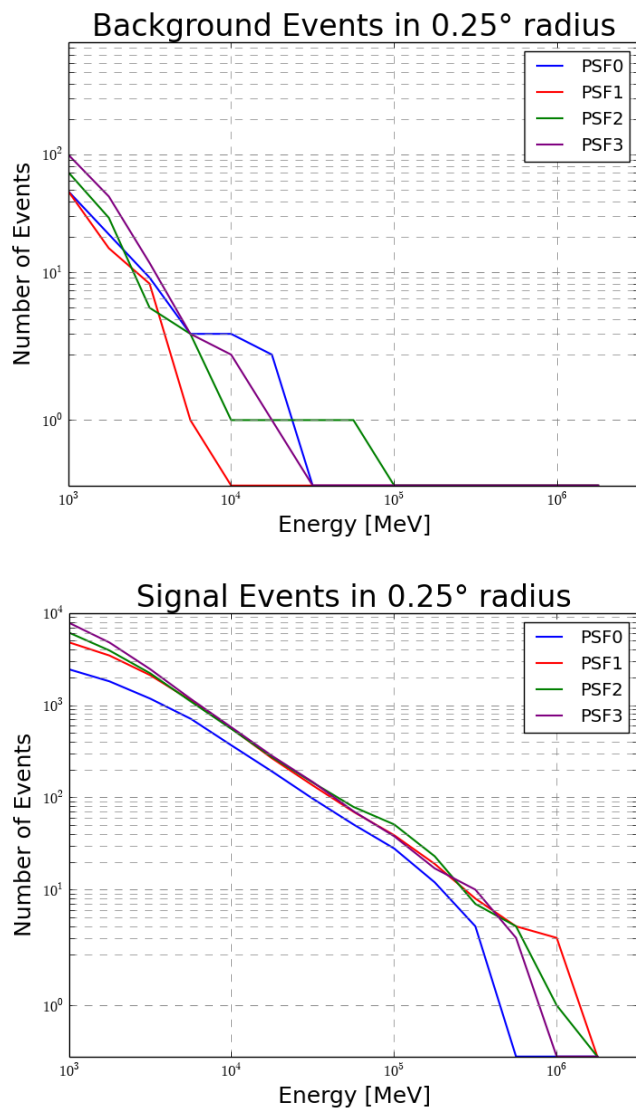


**Figure 4.6 & 4.7:** The energy dependence for the different PSF classes in the background (top) and signal (bottom) simulations in a 0.25° radius around the Crab pulsar. The logarithmic bin size is 0.25. The number of background events drops off much quicker than the number of signal events. For the signal, the composition is dominated by higher PSF classes at low energies, and by lower PSF classes at higher energies. For the background, the PSF composition is mostly determined by statistical fluctuation.

The influence of background photons is harder to predict. They do not only contribute through their PSF, but also through the difference in the position of their source. Since the exact position

# The Spatial Extension of the Inverse Compton Component of the Crab Nebula

## 4 Data Selection

---

can only be obtained for some but not all background sources, it is best to estimate the background photons as white noise to be subtracted from the data. The number of signal events is thus the difference between the number of recorded events ( $N_{events}$ ) and the number of background events. Through error propagation, this means the PSF of all background events contributes double, once as an error on all detected events and once as an error on the background events. The total error of the whole data set then adds up from their signal and background contributions:

$$\sigma_{Total}^2(N_{events}) = \sum_{i=1}^{N_{events}} \left( \frac{\sigma_{PSF}}{N_{events}} \right)^2 + \sum_{i=1}^{N_{bkg}} \left( \frac{\sigma_{PSF}}{N_{events}} \right)^2$$

$$\sigma_{Total}^2 = \frac{(N_{signal} + N_{bkg})\sigma_{PSF}^2 + N_{bkg}\sigma_{PSF}^2}{(N_{signal} + N_{bkg})^2} = \frac{N_{events} \left( 1 + \left( \frac{N_{signal}}{N_{bkg}} \right)^{-1} \right) \sigma_{PSF}^2}{N_{events}^2}$$

This total error estimate is not exact, but it does show the behavior needed for an effective discriminator. If the number of signal events increases, the total error improves. If the signal to background ratio improves, the total error improves. Lastly, if the PSF improves, the total error also improves. Therefore, the total error provides the means to distinguish between optimal and sub-optimal cuts.

Table 4.1 shows the calculated total error estimates for some of the considered cuts with the lowest total error estimate of their PSF class. The first three entries refer to the applied cuts, specifically the minimum energy in GeV, the minimum PSF class, and the maximum angular separation in degree still kept in the data set. The entries are determined as follows:

- $N_{cut}$ : the number of events in the data set after the pulsar phase cut.
- $N_{tot}$ : the number of events in the data set before the pulsar phase cut.
- $N_{bkg,cut}$ : the number of events in the background simulation before the pulsar cut weighted with the prefactor 0.4. The prefactor is a more exact estimate of the effect of the pulsar cut, as there is no pulsed emission in the background simulation.

# The Spatial Extension of the Inverse Compton Component of the Crab Nebula

## 4 Data Selection

---

- $N_{bkg,tot}$ : the number of events in the the background simulation without the prefactor, plus the number of expected pulsar events  $N_{pulsar}$ . This number is calculated from the number of events with and without pulsar phase cuts,  $N_{cut}$  and  $N_{tot}$  respectively. This assumes  $N_{cut}$  to be the true value of nebula events (plus other background) extended over the entire pulsar phase.  $N_{pulsar}$  is then simply the difference between recorded events and nebula events:  $N_{pulsar} = N_{tot} - 2.5 \cdot N_{cut}$ . In the unphysical case that the number of pulsar events is negative, because statistical fluctuations dominate, it is manually set to 0.
- PSF: the 68% containment radius of the pointlike simulation (see figure 4.5) in degree.
- $\sigma_{cut}$ : the variance of the entire sample  $\sigma$ , calculated from the given statistics with a pulsar phase cut applied.
- $\sigma_{tot}$ : the variance of the entire sample  $\sigma$ , calculated from the given statistics without a pulsar phase cut applied.

The first thing to notice is that the total error estimates are universally better without a cut on the pulsar phase than with a cut. This may hint at a systematic error in the calculation of the total error estimate, undervaluing the background statistics. Still, a region with a minimum total error estimate emerges, where it is smaller than  $3.00 \cdot 10^{-3}$ . As the total error is only an estimate, all cuts in this region are equivalent, and since the estimate may undervalue background, the cuts with the smallest remaining background was chosen. These were the cuts on events with energy lower than 18 GeV and a PSF Class worse than PSF2. Since this cut can be considered a high energy cut, the more restrictive  $0.25^\circ$  cut was chosen.

The final data set is then created by applying these cuts to the initial data set. Therefore photons in the final data set meet the following requirements:

- Energy  $E > 18$  GeV
- Angular Separation  $r < 0.250^\circ$

# The Spatial Extension of the Inverse Compton Component of the Crab Nebula

## 4 Data Selection

- PSF Class either PSF2 or PSF3

No cut is applied on the pulsar phase. The ephemeris and the piecewise data thus become obsolete, and all analysis is done exclusively on the full time data. This results in a slight increase of photon events compared to table 4.1 and the total number of photon events after cuts becomes 587. The phasogram at energies of the energy cut can be seen in figure 4.8

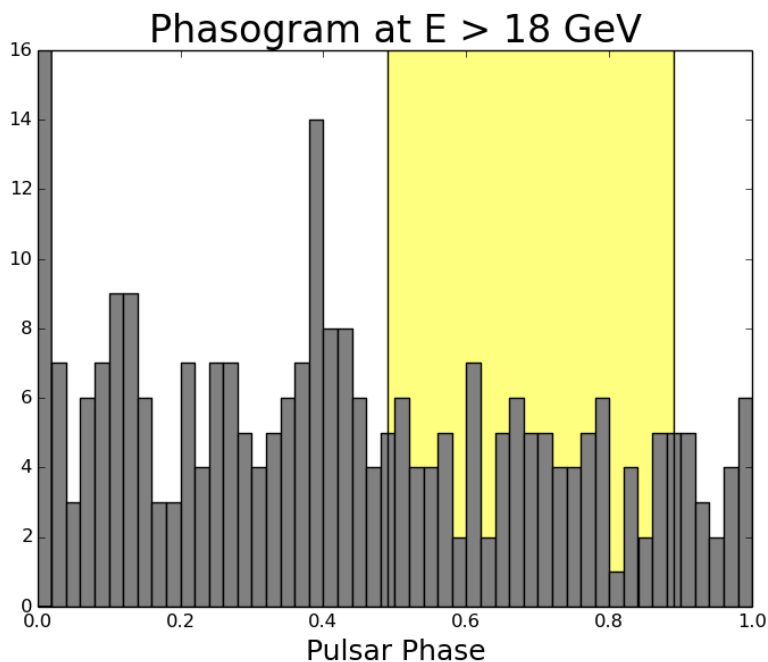


**Figure 4.8:** A phasogram of the Crab data set at energies above 18 GeV. The bin size is 0.02. The off-pulse region is marked yellow. At these energies, the contribution of the pulsar is significantly reduced, and the number of pulsar events is hard to determine, due to large statistical uncertainties.

PSF cut [°]	E cut [GeV]	r cut [°]	$N_{cut}$	$N_{tot}$	$N_{bkg,cut}$	$N_{bkg,tot}$	PSF [°]	$\sigma_{cut}$ [°]	$\sigma_{tot}$ [°]
PSF0	5.6	0.25	870.0	4107.0	4.0	1942.0	0.1961	0.00666	0.00371

**The Spatial Extension of the Inverse Compton Component of the Crab Nebula**  
*4 Data Selection*

PSF0	5.6	0.5	1007.0	4769.0	12.8	2283.5	0.1960	0.00622	0.00345
PSF0	10	0.25	556.0	2056.0	2.4	672.0	0.1459	0.00620	0.00371
PSF0	10	0.5	623.0	2323.0	4.4	776.5	0.1459	0.00587	0.00350
PSF1	5.6	0.25	717.0	3395.0	2.8	1609.5	0.1400	0.00524	0.00292
PSF1	5.6	0.5	773.0	3682.0	9.2	1772.5	0.1400	0.00506	0.00281
PSF1	10	0.25	456.0	1689.0	1.2	552.0	0.1021	0.00479	0.00286
PSF1	10	0.5	480.0	1774.0	3.2	582.0	0.1021	0.00468	0.00279
PSF2	5.6	0.25	480.0	2268.0	2.4	1074.0	0.1144	0.00524	0.00292
PSF2	5.6	0.5	498.0	2356.0	5.6	1125.0	0.1144	0.00516	0.00287
PSF2	10	0.25	300.0	1129.0	1.2	382.0	0.0825	0.00477	0.00284
PSF2	10	0.5	307.0	1150.0	1.6	386.5	0.0825	0.00472	0.00281
PSF2	18	0.25	188.0	555.0	0.8	87.0	0.0629	0.00460	0.00287
PSF2	18	0.5	192.0	562.0	0.8	84.0	0.0629	0.00455	0.00284
PSF3	10	0.25	150.0	576.0	0.8	203.0	0.0679	0.00556	0.00329
PSF3	10	0.5	152.0	580.0	1.2	203.0	0.0679	0.00553	0.00327
PSF3	18	0.25	89.0	282.0	0.4	60.5	0.0503	0.00534	0.00330
PSF3	18	0.5	91.0	285.0	0.4	58.5	0.0503	0.00528	0.00327

**Table 4.1:** Calculations of the total error estimates

## 5 Data Analysis:

All histograms in this section and the next sections were calculated for all 21 template models. The portrayed histograms only show an excerpt of these 21 models, including the smallest, middle, and largest template, as well as the best fit. The full histograms for all 21 models can be found in Appendix C with the exception of the partial data plots in section 5.2.

### 5.1 Angular Separation of the Crab Nebula:

There is no reason to assume the Crab nebula to be symmetrical around the Crab pulsar. It is possible for the nebula's center of gravity to slightly deviate from the location of the pulsar. Therefore it has to be calculated separately via:

$$\langle RA \rangle = \frac{\sum_{i=1}^N RA_i}{N}$$

This gives a Crab nebula center of  $RA = 83.6331^\circ$ ,  $DEC = 22.0220^\circ$ , located at a slightly larger declination than the Crab pulsar at  $RA = 83.6331^\circ$ ,  $DEC = 22.0145^\circ$ . The angular separation to center will from this point onwards be calculated in respect to the nebula's center of gravity.

It is worth mentioning, that this creates a slight bias on events closer to the Crab pulsar, as the cut on the data set was performed in regards to the pulsar position. However, the difference in pulsar and nebula position is small in comparison to the cut radius of  $0.25^\circ$ , and concerning a region with the lowest probability distribution of photons, so that this bias can be neglected.

Although the center of Mkn 421 should be Mkn 421 itself, its center of gravity is also calculated, to be consistent with the analysis. The center of gravity is determined as  $RA = 166.120^\circ$ ,

# The Spatial Extension of the Inverse Compton Component of the Crab Nebula

## 5 Data Analysis:

---

$DEC = 38.207^\circ$ , slightly different from the Mkn 421 location  $RA = 166.114^\circ$ ,  $DEC = 38.2088^\circ$ .

After the final cuts were applied, a data sample of 587 photon events remains. An attempt was made to distribute these sources onto PSF classes and sources. The distribution onto PSF classes could be done exact, as these are recorded in the data, while the attribution to sources was done based on the ratios found in table 4.1 (first the ratio nebula to pulsar, then PSF2 to PSF3, rounded to the nearest integer). The distribution of these remaining events onto PSF classes and sources can be seen in table 5.1.

Crab Events	Nebula	Pulsar	Background
PSF2	241	44	1
PSF3	254	46	1

**Table 5.1:** Distribution of Crab events to sources

Figure 5.1 shows a histogram of the Crab nebula photon distribution and stacked distributions for all simulated model templates in regards to the angular separation  $r$  in bins of  $0.01^\circ$ , including the best fit in black. The model template distributions were created from stacks of a PSF2 template simulation, a PSF3 template simulation, a PSF2 pointlike simulation around the Crab pulsar, and a PSF3 pointlike simulation pulsar. The latter two were included to properly simulate the pulsar background. Background from other sources was considered small enough to be neglected.

All simulations were weighted to match the number of data events of their respective category. The PSF2 template simulation was weighted to match 242 PSF2 nebula + background events, the PSF3 template simulation was weighted to match 255 PSF3 nebula + background events, the PSF2 pointlike simulation was weighted to match 44 PSF2 pulsar events, and the PSF3 pointlike simulation was weighted to match 46 PSF3 pulsar events. The overall weighting is in the size of  $1/200$ .

The different template simulations show two defining characteristics, from which they can be

# The Spatial Extension of the Inverse Compton Component of the Crab Nebula

## 5 Data Analysis:

---

**Figure 5.1:** A histogram of the angular separation distribution of Crab data to its center of mass. The simulated templates shown correspond to the smallest (red), medium-sized (yellow), and largest (green), as well as the best fit (black).

most easily distinguished: the location of their peak photon bin and the event count in the first bin. For larger template sizes, the peak flux value is still centered around 0, but the overall peak flattens. This causes the photon count in the first bin, covering the smallest area around the center, to decrease with increased template size, as well as the shift of the peak value, denoted by flux times area, to shift further outward. Both these characteristics will ultimately be the most influential in distinguishing the different models.

To determine the template which best fit the data, a binned likelihood analysis is performed and the maximum likelihood determined. The likelihood is calculated in the following way:

The probability to detect  $k$  photons in any bin with an expectation value of  $\lambda$  follows a Poisson distribution:

$$p_i = \frac{\lambda^k e^{-\lambda}}{k!}$$

The total probability  $P$  to detect  $k_i$  photons in all  $i$  bins, is then simply the product of the individual probabilities:

$$P_i = \prod_{i=1}^N p_i$$

From this, the likelihood  $L$  can be calculated. There are a number of ways in use to define the likelihood. For this thesis, the definition of the likelihood is given by:

$$L = -\log(P_i) = -\sum_{i=1}^N \log(p_i)$$

Through this definition, the likelihood reaches a global minimum for the same distribution, for which the total probability reaches a global maximum. This value is then called maximum estimated likelihood (with the name originating from a different definition of likelihood; in this con-

# The Spatial Extension of the Inverse Compton Component of the Crab Nebula

## 5 Data Analysis:

---

text, the used definition of the likelihood is then referred to as negative logarithmic likelihood).

According to Wilks's theorem, the difference between different model likelihoods follows a  $\chi^2$  distribution with the same  $n$  degrees of freedom as were present in the different models. As the most sensible comparison is to the best fit  $L_{min}$ , this is:

$$\chi^2(n) = 2(L_x - L_{min})$$

In this case, the only degree of freedom is the radius of the model template, and thus  $n = 1$ . A 95% confidence interval is then defined by the value at which the cumulative density function of the  $\chi^2$  distribution reaches 95%. The exact value can be looked up in most statistic textbooks (Roe 1992):

$$\int_0^{\chi^2} \chi'^2(n=1) dx = 0.95 \Leftrightarrow \chi^2 = 3.84$$

Thereby, the 95%-confidence interval is defined by a likelihood difference of:

$$\Delta L_{95} = 1.92$$

Figure 5.2 shows the calculated likelihoods of all model templates. The threshold of the 95% confidence interval as well as the exclusion region are marked in red. The maximum estimated likelihood is found for the  $0.04^\circ$  radius template, with the 95% confidence interval ranging from  $0.03^\circ$  to  $0.05^\circ$ . The deviation from the pointlike template simulation is  $\Delta L = 18.2$  and corresponds to a p-value of  $p < 10^{-4}$ . This proves the size of the Crab nebula starts increasing from a pointlike source to an extended source again, upon the change of the dominating spectral component from synchrotron radiation to inverse Compton radiation.

The length of the radio Crab nebula's minor and major axis are roughly 4.6 and 7 arcminutes respectively, which corresponds to a radial length of roughly  $0.038^\circ$  and  $0.058^\circ$  in these directions. These two values are the upper and lower limits for the expected Crab nebula radius and are entirely consistent with the calculated 95% confidence interval. It is therefore plausible, that the detected Crab nebula inverse Compton radiation originates from the same electron population as the Crab nebula's radio synchrotron emissions. The exact size of the inverse Compton Crab

## **The Spatial Extension of the Inverse Compton Component of the Crab Nebula**

### *5 Data Analysis:*

---

nebula cannot be resolved, and it remains equally possible to originate from a smaller or even larger region, in direction of the minor axis, than the size of the radio Crab nebula.

**The Spatial Extension of the Inverse Compton Component of the Crab Nebula**  
*5 Data Analysis:*

---

**The Spatial Extension of the Inverse Compton Component of the Crab Nebula**  
*5 Data Analysis:*

---

**The Spatial Extension of the Inverse Compton Component of the Crab Nebula**  
*5 Data Analysis:*

---

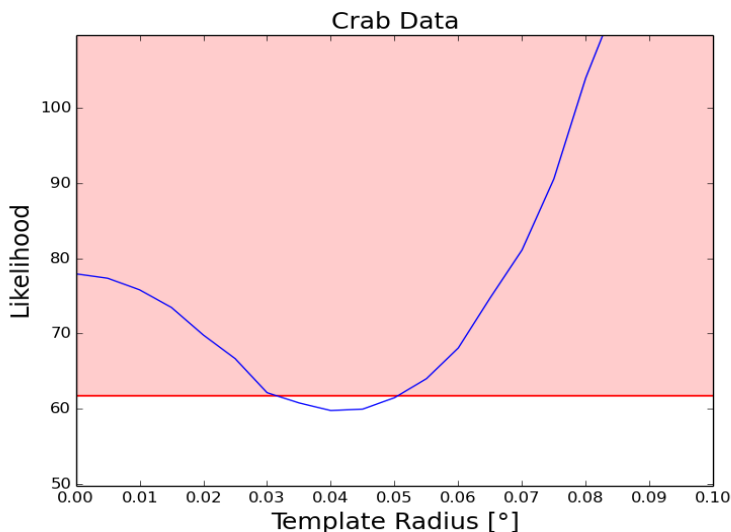


**Figure 5.2:** The likelihood for each model template as a function of the model template radii for Crab data. The 95% exclusion region is marked in red. The maximum estimated likelihood is located at  $0.040^\circ$ . The pointlike template can be excluded with a certainty  $p < 10^{-4}$ .

## 5.2 Angular Separation of Markarian 421:

For confirmation of the analysis, the same analysis is applied to Markarian 421. As a blazar, Markarian 421 is expected to appear as a pointlike source, and a valid analysis should be able to confirm this. In the final Mkn 421 data set, 544 events, distributed into 292 PSF2 and 252 PSF3 events remain. These events were entirely believed to be signal, as the Mkn 421 background simulations had not a single recorded photon event left after cuts, which is not unlikely for an extragalactic source.

Figure 5.3 is the same histogram as for the Crab, with the same bin size, only showcasing the Mkn 421 data and Mkn 421 simulations instead. Again, simulations were weighted by PSF class to match their respective number of Mkn 421 data events. The corresponding calculated likelihoods can be seen in figure 5.4.

The first thing to notice is that the likelihood plot is not monotonous up to the minimum, located at the  $r = 0.020^\circ$  template. The minimum likelihood drops off very quickly when comparing the  $0.015^\circ$  and the  $0.020^\circ$ . This is a hint that the given models may not describe the Mkn 421 data

# The Spatial Extension of the Inverse Compton Component of the Crab Nebula

## 5 Data Analysis:

---

very well, since a likelihood analysis states nothing about the absolute goodness of fit for the individual models. Another hint comes from the absolute value of the likelihood when compared to that of the Crab. While it is dangerous to assign too much importance to the absolute value of a likelihood, the fact that the Crab and the Mkn 421 analysis use the same number of bins and almost the same number of events does mean, their absolute likelihoods should be comparable. That the minimum likelihood of Mkn 421 is a value of 2 higher than the minimum likelihood of the Crab nebula again hints at a goodness of fit for the Mkn 421 data which is generally worse than for the Crab.

The 95% confidence interval in this case only ranges from  $0.020^\circ$  to  $0.025^\circ$  and specifically excludes a pointlike template. This means the analysis process is unable to confidently reproduce Mkn 421 as a point source. To still consider the used analysis process valid, an explanation for this inability needs to be found.

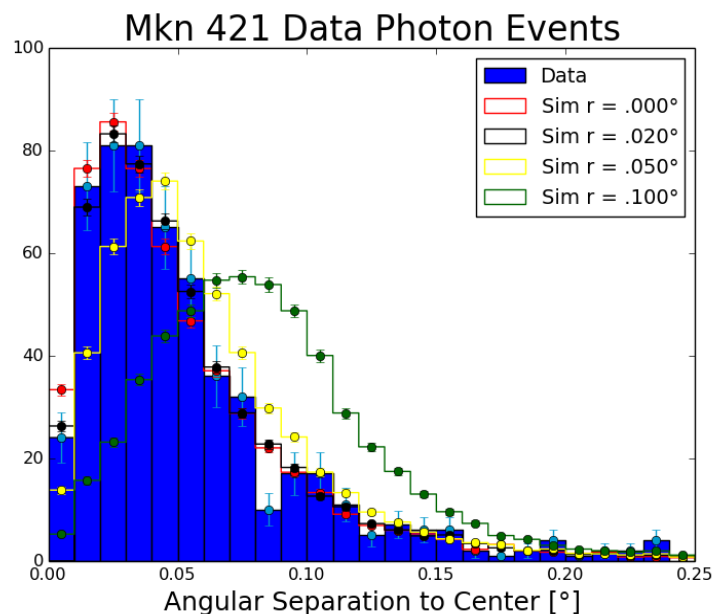


**Figure 5.3:** A histogram of the angular separation distribution of Mkn 421 data to its center of mass. The simulated templates shown correspond to the smallest (red), medium-sized (yellow), and largest (green), as well as the best fit (black).

# The Spatial Extension of the Inverse Compton Component of the Crab Nebula

## 5 Data Analysis:

---

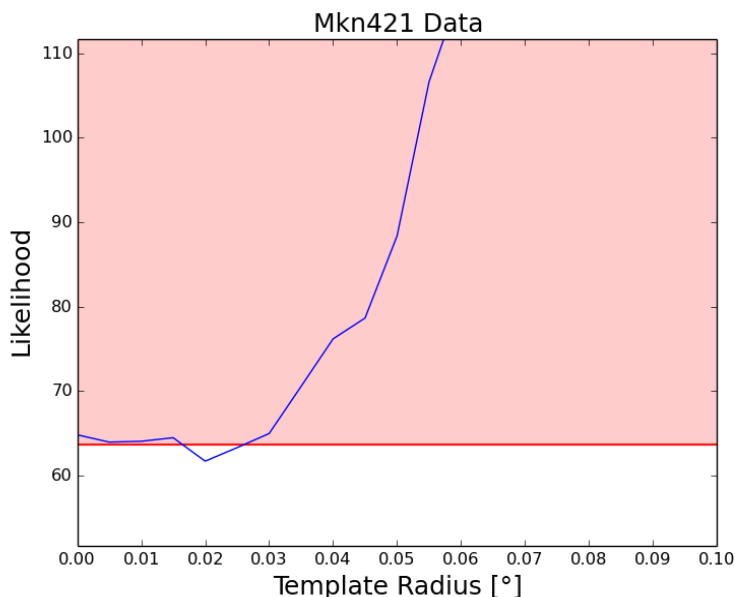


**Figure 5.4:** The likelihood for each model template as a function of the model template radii for Mkn 421 data. The 95% exclusion region is marked in red. The maximum estimated likelihood is located at  $0.020^\circ$ . The pointlike template is specifically excluded.

As mentioned before, the bin most sensitive to the pointlike template is the first bin with the bin edges  $0.00^\circ < r < 0.01^\circ$ . This is also one of the bins with the most deviation from the pointlike template. The other bins with an increased distinctive power are also bins with smaller  $r$ , since this is where the photon peak values for the smaller model templates are located. To account for these bins specifically, a subsample of the data only considering events up to  $r < 0.05^\circ$  and  $r < 0.10^\circ$  is analyzed, and the simulations are then reweighted to the number of remaining events. The corresponding histograms and likelihood functions can be seen in figures 5.5 through 5.8.

The likelihoods for these subsamples are much more compatible with the pointlike template than before, although this is to be expected due to an increase in uncertainty through the decrease in data. The 95% confidence intervals in both cases include the pointlike template and range from  $0.000^\circ$  to  $0.030^\circ$ . This indicates that the main problem of reconstruction emerges from the outliers of photon events with a high reconstructed angular separation and this effect may be dimin-

# The Spatial Extension of the Inverse Compton Component of the Crab Nebula

## 5 Data Analysis:

---

ished by cutting on these events. However, it can not be excluded, that the total error comes from errors in both the small angular separation and the large angular separation region piling up.

Two other subsamples were created: one with only PSF2 events, the other with only PSF3 events. Since their individual PSFs differ considerably, these samples could illuminate problems in the reconstruction of individual events. The histograms and likelihoods of these subsamples can be seen in figures 5.9 through 5.12.

Due to its lower PSF, the PSF3 subsamples appears much more peaked around smaller angular separation values. Although the resolution of this subsample is still far too large to observe any substructures, the existence of such substructures would show more dominantly in the PSF3 sample.

The likelihoods of the PSF2 and PSF3 subsamples do not differ much from the likelihoods found for the full data set, although their change in values for the different templates appears much more erratic. Their 95% confidence intervals include, in the case of the PSF2 sample, the pointlike, the  $0.005^\circ$  template, as well as the  $0.020^\circ$  to  $0.030^\circ$  templates, and in the case of the PSF3 sample, only the  $0.010^\circ$  template, as well as the  $0.020^\circ$  template. It is impossible to make out a difference between the overall reconstruction of PSF2 and PSF3 events.

# The Spatial Extension of the Inverse Compton Component of the Crab Nebula

## 5 Data Analysis:

---

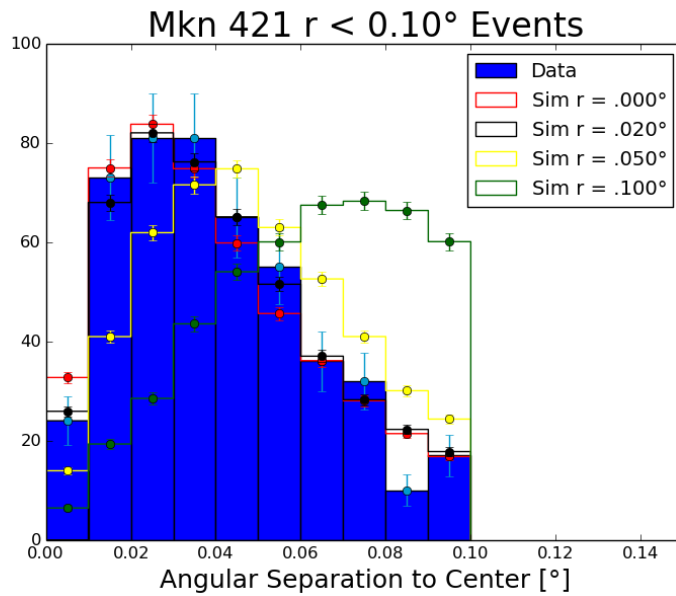
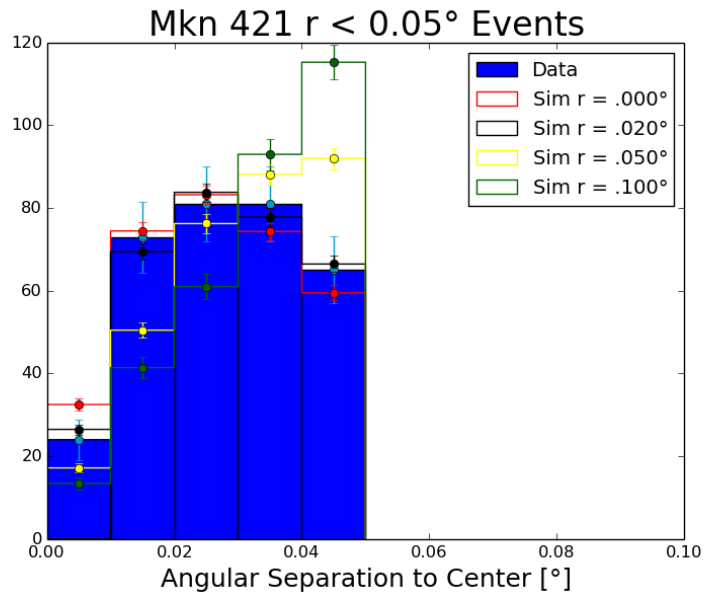
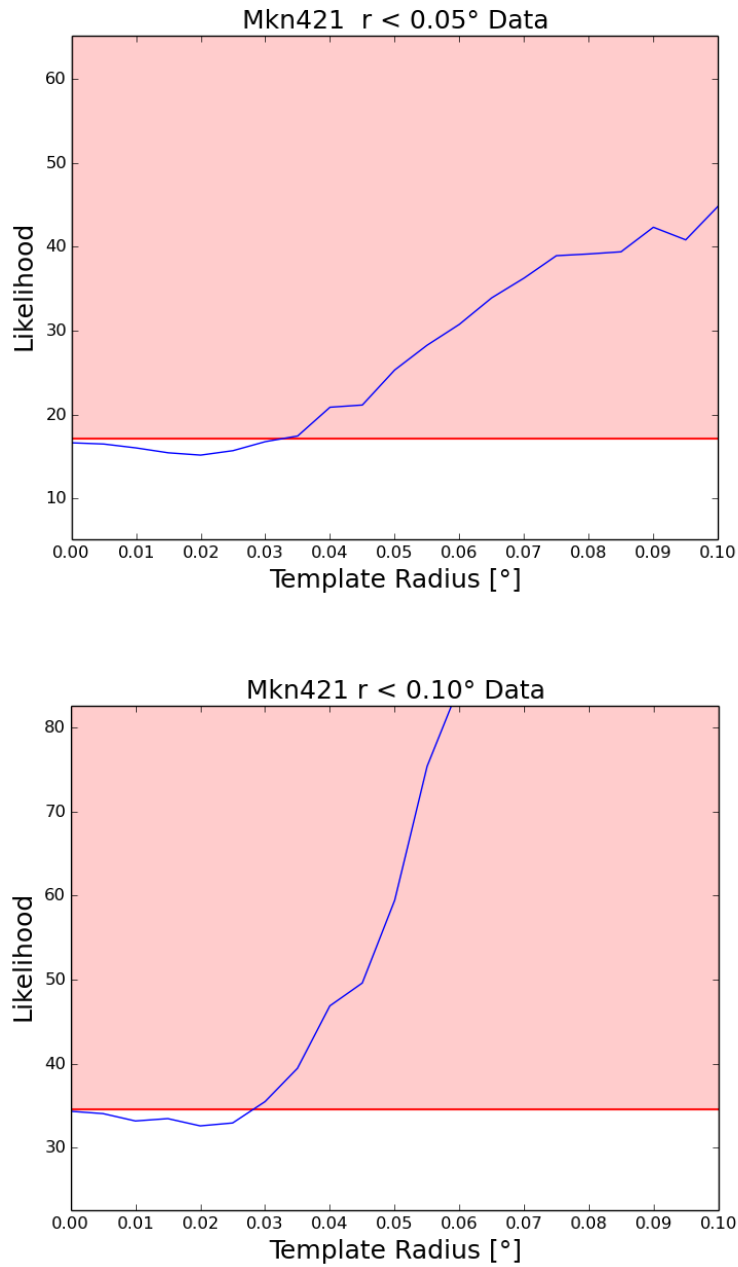


Figure 5.5 & 5.6: Histogram of the angular separation distribution of Mkn 421 data only evaluating events in a  $0.05^\circ$  radius (top) and  $0.10^\circ$  radius (bottom).

# The Spatial Extension of the Inverse Compton Component of the Crab Nebula

## 5 Data Analysis:

---



**Figure 5.7 & 5.8:** Likelihoods for each model template as a function of the model template radii for  $r < 0.05^\circ$  cut (top) and  $r < 0.10^\circ$  cut (bottom) Mkn 421 data. The 95% exclusion region is wider than for the full data set, but still peaks at  $0.020^\circ$ .

# The Spatial Extension of the Inverse Compton Component of the Crab Nebula

## 5 Data Analysis:

---

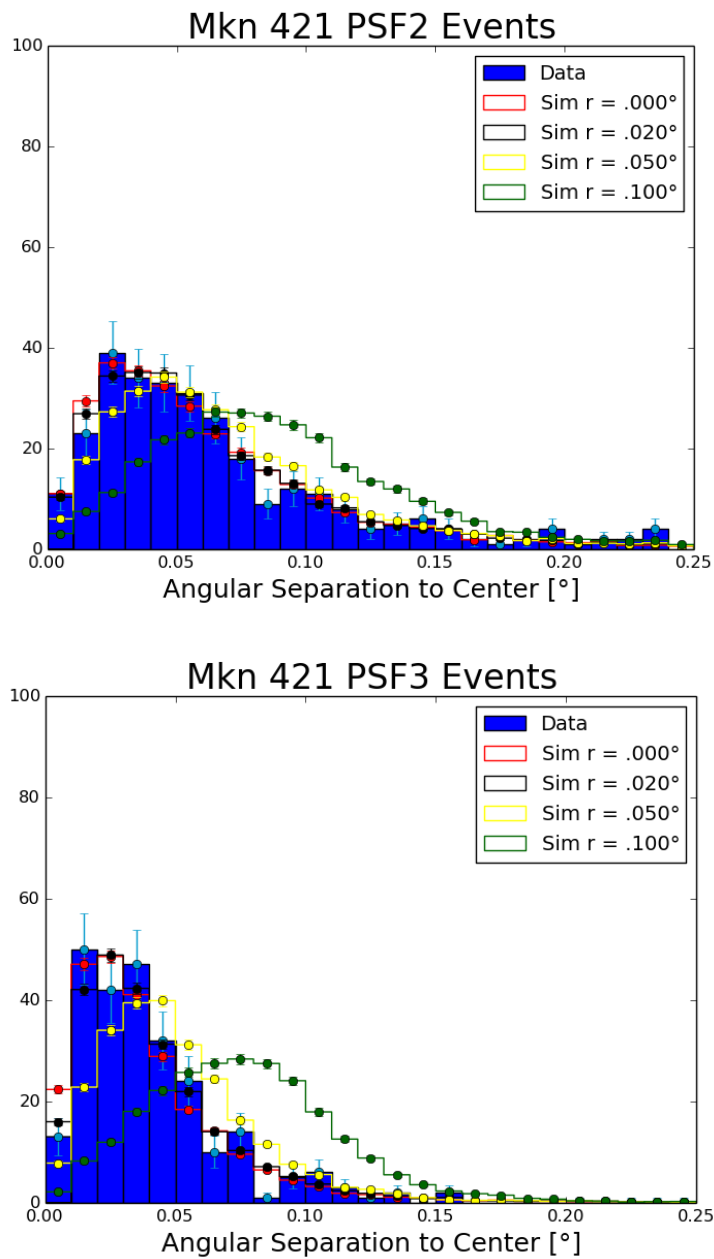


**Figure 5.9 & 5.10:** Histogram of the angular separation distribution of Mkn 421 data only evaluating PSF2 events (top) and PSF3 events (bottom) respectively. The PSF3 distribution is more peaked in both data as well as simulation, due to its improved PSF.

# The Spatial Extension of the Inverse Compton Component of the Crab Nebula

## 5 Data Analysis:

---

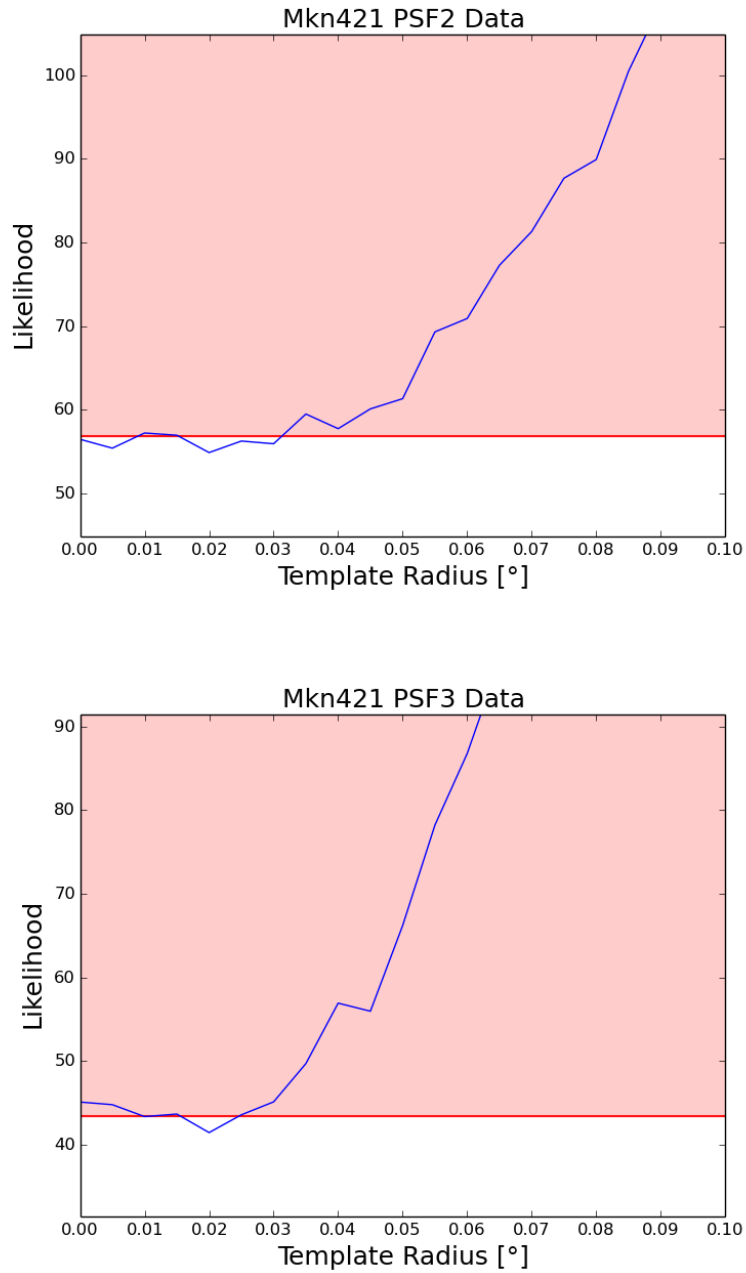


**Figure 5.11 & 5.12:** Likelihoods for each model template as a function of the model template radii for PSF2-only (top) and PSF3-only (bottom) data. Neither subsample shows significant improvement in reconstructing Mkn 421 as a point source over the full data set.

## The Spatial Extension of the Inverse Compton Component of the Crab Nebula

### 5 Data Analysis:

---

Lastly, a direct comparison between the Crab data and the Mkn 421 data is made. Figure 5.13 shows a histogram of both data sets in direct comparison, with the Mkn 421 data weighted to match the number of Crab events. The weighting was done differently from previous histograms. To compensate for the difference in spectra of the Crab nebula and Markarian 421, all photons were partitioned into energy ranges alongside their PSF classes, and each of these partitions weighted individually. This was done because photons inside one energy range with the same PSF class correspond to roughly the same PSF. The energy ranges considered were  $E_1 = 18 - 32$  GeV,  $E_2 = 32 - 56$  GeV, and  $E_3 = 56 - 2000$  GeV. The specific event count and rates can be seen in table 5.2. As these weights ( $w_1, w_2, w_3$ ) are all highly correlated, for the purposes of error propagation a universal weighting of  $w = 1.08$ , which is the ratio between all Crab events to all Mkn 421 events, is assumed.

Source	PSF Class	$E_1$	$E_2$	$E_3$	$w_1$	$w_2$	$w_3$
Crab	PSF2	136	68	82	1.00	1.00	1.00
	PSF3	143	80	78	1.00	1.00	1.00
Mkn 421	PSF2	110	90	92	1.24	0.76	0.89
	PSF3	105	71	76	1.36	1.13	1.03

**Table 5.2:** Distribution of Crab and Mkn 421 events to energies and PSF classes, and their according weights

A chi-squared test is performed for the first ten bins, to compare the goodness-of-fit. In the first ten bins, the photon count is deemed large enough to assume Poissonian errors. Therefore, the total error on each bin is:

$$\sigma_{tot} = \sqrt{(\sqrt{N_{crab}})^2 + (w\sqrt{N_{Mkn421}})^2}$$

The  $\chi^2$  statistic then becomes:

# The Spatial Extension of the Inverse Compton Component of the Crab Nebula

## 5 Data Analysis:

---

$$\chi^2 = \frac{(N_{crab} - N_{Mkn421})^2}{\sigma_{tot}^2}$$

Between the Crab and Mkn 421,  $\chi^2$  is  $\chi^2 = 10.48$ , which shows high goodness-of-fit for  $n = 10$  degrees of freedom. This is unsurprising, as Mkn 421 data as a model has very large uncertainties, which are even scaled up by the weighting, and is hence easy to fit to any data. The significance of this fit is therefore very low. It is worth noting however, that the peak photon value for the Crab is located at higher  $r$  values than that of Mkn 421, which does indicate that it is larger. Other than this, no definite conclusions can be drawn.

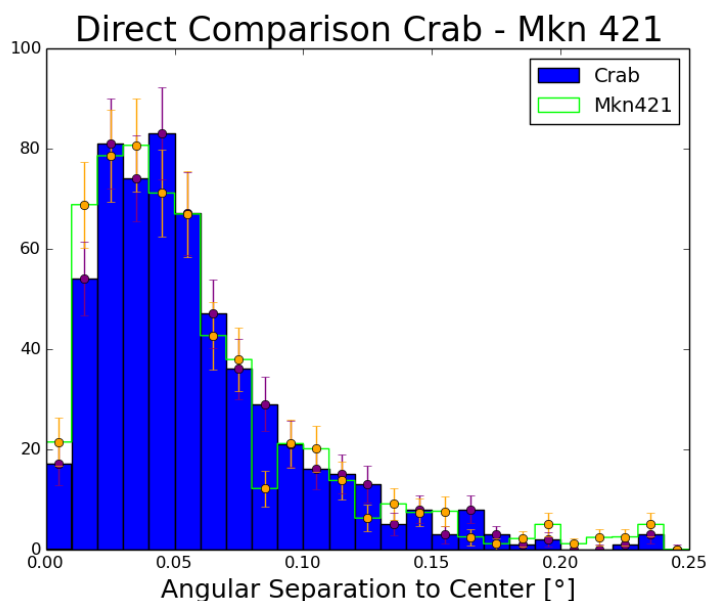


**Figure 5.13:** A histogram directly comparing Crab data to Mkn 421 data. Crab error bars are drawn purple, Mkn 421 error bars were drawn orange. All errors are assumed to be Poissonian.

All of the data subsamples show the same estimated maximum likelihood for the  $0.020^\circ$  template, leading to the conclusion that the inability to reproduce Mkn 412 as a point source originates from the analysis process as a whole. This can be interpreted as a systematic uncertainty on the modeling process as a whole, although it can not be said whether this results in a scaling error

# The Spatial Extension of the Inverse Compton Component of the Crab Nebula

## 5 Data Analysis:

---

or shift in size. Ultimately, this would lower the validity of the Crab analysis significantly.

An alternative explanation is provided by Chen, Buckley, and Ferrer (2015). Their analysis of 24 low redshift blazars ( $z < 0.5$ ) around  $\sim 1$  GeV found an excess of their spatial extension over pointlike sources. Chen, Buckley, and Ferrer interpret these findings as gamma-ray pair halos around the blazar. Gamma-rays from these halos may still be present at the analysis energies  $> 18$  GeV, and since Mkn 421 is a source very close to earth ( $z = 0.031$ ), the size of its halo could be particularly big. In this interpretation, Mkn 421 cannot be considered a point source in the eyes of a high-energy Fermi LAT analysis.

This leads to the final conclusion that Mkn 421 is a poor choice of a reference point source, as it is dubious whether it appears as a gamma-ray point source to Fermi LAT to begin with. It is best to regard the Crab analysis completely independently, and proceed without complete confirmation of the analysis process, and let its validity be determined by the first principles from which it is derived.

## 5.3 Crab Minor and Major Axis:

Since the radio Crab nebula has the shape of an ellipsis, the inverse Compton nebula is expected to have the same shape, and it may be possible to spot a difference between the Crab nebula's photon distribution along the major axis and along the minor axis. In order to evaluate this, it is necessary to transform the photon coordinate system into a coordinate system defined by these axes.

The original coordinate system is defined as:

$$r = \begin{pmatrix} \cos(\theta)\cos(\varphi) \\ \cos(\theta)\sin(\varphi) \\ \sin(\theta) \end{pmatrix},$$

with  $\varphi$  the right ascension and  $\theta$  the declination.

# The Spatial Extension of the Inverse Compton Component of the Crab Nebula

## 5 Data Analysis:

This can be transformed into the minor-major-axis system through three rotations: first along the z-axis, to align the origin with the Crab right ascension, then along the y-axis to align the origin with the Crab declination, and then along the x-axis, to align the two axes with the minor and the major Crab axis respectively. The angles for these rotations are  $83.6331^\circ$ ,  $22.0145^\circ$ , and  $30^\circ$ , with the last value being taken from Hester (2008).

$$r' = \begin{pmatrix} \cos(\alpha)\cos(\beta) \\ \cos(\alpha)\sin(\beta) \\ \sin(\alpha) \end{pmatrix} = \begin{pmatrix} \cos(\theta)\cos(\varphi) \\ \cos(\theta)\sin(\varphi) \\ \sin(\theta) \end{pmatrix} \cdot D_z \cdot D_y \cdot D_x$$

By solving this equation, the angles for the Crab major axis  $\alpha$  and the minor axis  $\beta$  are :

$$\alpha = \sin^{-1}\left([\sin(\theta)\cos(\theta_{Crab}) - \cos(\theta)\sin(\theta_{Crab})\cos(\Delta\varphi)]\cos(30^\circ) - \cos(\theta)\sin(\Delta\varphi)\sin(30^\circ)\right)$$

$$\beta = \tan^{-1}\left(\frac{[\sin(\theta)\cos(\theta_{Crab}) - \cos(\theta)\sin(\theta_{Crab})\cos(\Delta\varphi)]\sin(30^\circ) - \cos(\theta)\sin(\Delta\varphi)\cos(30^\circ)}{\cos(\theta)\cos(\Delta\varphi)\cos(\theta_{Crab}) + \sin(\theta)\sin(\theta_{Crab})}\right)$$

Figures 5.14 through 5.17 show the histograms and likelihoods for the Crab data photon distribution from  $-0.25^\circ$  to  $0.25^\circ$  along the major and minor Crab axes. Since  $\alpha$  and  $\beta$  can take on negative values, the bin size has been increased to  $0.02^\circ$  to amount to the same number of total bins. This also makes the distribution of  $\alpha$  and  $\beta$  much more peaked and centered around 0. The bins by which the different models can best be distinguished are therefore the ones close to 0.

The simulation histograms reveal a slight asymmetry for both  $\alpha$  and  $\beta$ , which is less present in the Crab data, due to higher fluctuations. This asymmetry can be attributed to the Crab pulsar, which is not located at 0 due to its difference from the Crab nebula center of mass. Through this, the effects of Crab pulsar background on the major and minor axis distribution can be expected to be much more significant than in the case of the angular separation distribution, and the systematic uncertainties on the center of the Crab nebula, as well as the number of Crab pulsar events should not be completely neglected.

The maximum estimated likelihoods and the 95% confidence intervals for the major and minor axes are slightly shifted from the angular separation likelihoods and from each other. The maximum estimated likelihoods are  $0.040^\circ$  in the case of the minor axis, and  $0.045^\circ$  in the case of

## The Spatial Extension of the Inverse Compton Component of the Crab Nebula

### 5 Data Analysis:

---

the major axis. The 95% confidence intervals range from  $0.020^\circ$  to  $0.045^\circ$  in the case of the minor axis, and from  $0.030^\circ$  to  $0.050^\circ$  in the case of the major axis.

The major axis can be identified as larger than the minor axis by its maximum estimated likelihood, as well as the lower and upper limits of its 95% confidence interval. In the case of the minor axis, the confidence interval complies with its radio Crab nebula extension of  $0.038^\circ$ , while for the major axis, it does not (the major axis Crab nebula extension is  $0.058^\circ$ ). The confidence intervals of the major and minor axis have an overlap region, which is much larger than the difference in their maximum estimated likelihood. This means the statistical error on the extension of the nebula in its minor and major axis is too large to tell them apart, and that the difference in size may be entirely due to chance.

In conclusion, it can neither be said that  $\alpha$  and  $\beta$  correspond to the major and minor axes of the inverse Compton Crab nebula, nor that there even is a significant difference from a circular shaped projected Crab nebula. But since all assumed models were circular, this is not surprising. To resolve any substructures of the inverse Compton, more complex models are needed, which account for its expected elliptical shape specifically. All that can be concluded from this analysis is that it may be worth repeating the analysis with such improved models.

# The Spatial Extension of the Inverse Compton Component of the Crab Nebula

## 5 Data Analysis:

---

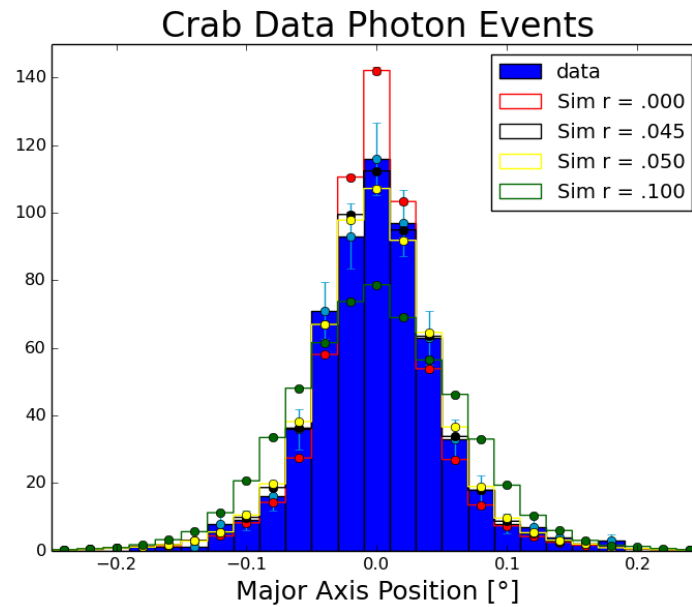
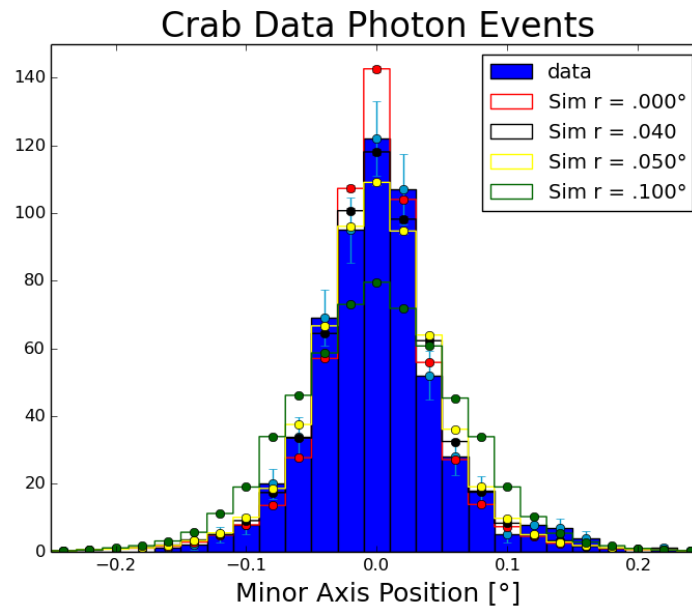


**Figure 5.14 & 5.15:** Histograms of the distribution of Crab data along its minor (top) and its major (bottom) axis. The bin size is increased to  $0.2^\circ$  to maintain the same number of bins. The simulated templates shown correspond to the smallest (red), medium-sized (yellow), and largest (green), as well as the best fit (black). A slight asymmetry in the simulation templates is noticeable.

# The Spatial Extension of the Inverse Compton Component of the Crab Nebula

## 5 Data Analysis:

---

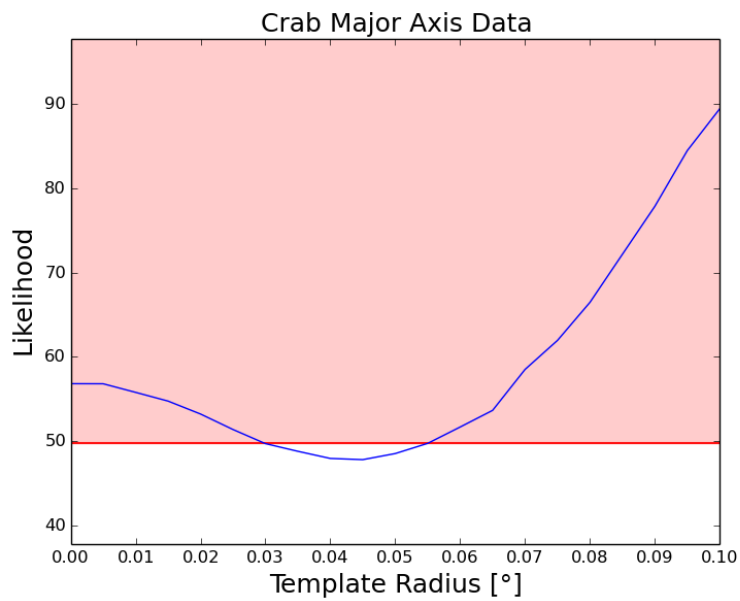
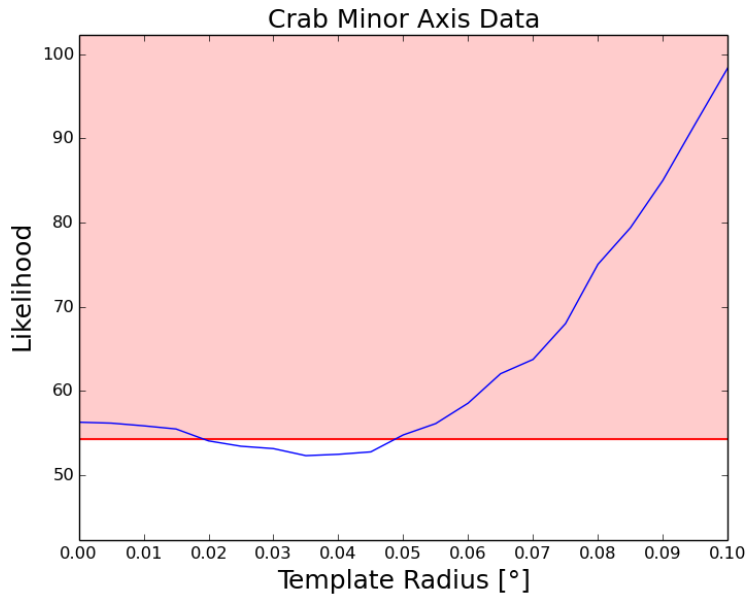


**Figure 5.16 & 5.17:** Likelihoods for each model template distribution along the minor (top) and major (bottom) axis as a function of the model template radii. The maximum estimated likelihood is slightly larger for the major axis, but the 95% confidence intervals of both are compatible with each other.

## 6 Results and Outlook

For the inverse Compton component of the Crab nebula, a spatial extension of the size  $r = 0.040^\circ$  was found, with a 95% confidence interval ranging from  $0.035^\circ$  to  $0.050^\circ$ . The point-like source template, which describes the spatial extension of the Crab nebula's synchrotron component extension, could be excluded with a significance of  $p < 10^{-4}$ . This proves that the high-energy synchrotron radiation and the high-energy inverse Compton radiation of the Crab nebula originate from different electron populations. In the case of the inverse Compton component, the electron population is most likely identical to that of the radio synchrotron component. The resolution of this analysis was not enough to determine, whether the size of the inverse Compton nebula and the radio synchrotron nebula were identical, or whether one is larger than the other. Therefore, no additional insight on the existence of cold electron populations or electron populations with a small gamma-factor was gained.

The measurement of the inverse Compton Crab nebula extensions along its major and minor axis found a statistically insignificant difference between the two, with the major axis, with an extension of  $0.045^\circ$ , being slightly larger than the minor axis, with an extension of  $0.040^\circ$ . Their 95% confidence intervals of  $0.030^\circ$  to  $0.050^\circ$  in the case of the major, and  $0.020^\circ$  to  $0.045^\circ$  in the case of the minor axis are compatible with each other, and in the case of the minor axis, compatible with its radio synchrotron extension of  $0.038^\circ$ . The extension along the major axis of the radio synchrotron nebula of  $0.058^\circ$  is excluded by the upper limit of the 95% confidence interval. This may be attributed to the limitations of the models used. More complex models are needed to resolve any of the inverse Compton nebula's substructures. The simplest of these models would be an ellipsoidal shape, with a varying size minor axis, major axis, and angle. Since these models include three free parameters, the necessary number of models in such an analysis would increase significantly.

# The Spatial Extension of the Inverse Compton Component of the Crab Nebula

## *6 Results and Outlook*

---

One proof this analysis owes is that of its validity to identify point sources. The analysis process could not reproduce Markarian 421 as a point source, and regardless of whether that is due to a systematic error, or to the presence of a halo around Markarian 421, a confirmation of the analysis process with a different point source would be desirable. However, bright point sources in the gamma-ray sky are few and far between, and the brightest, such as the Velar pulsar, are all galactic and thus contaminated with background. Extragalactic sources tend to have a significantly lower flux than the Crab nebula, which would provide an additional challenge to the analysis merely through this.

One way such a new point source could be analyzed would be through the improvement of the applied cuts. The cuts used in this analysis are very strict in that they cut on any photon which does not meet any one of the cut requirements. By performing individual cuts on each of the PSF classes, one would be able to include high-energy PSF0 events and low-energy PSF3 events with a comparable point spread function in the data, and get much improved statistics. The same way, cuts on the pulsar phase could be applied only in energy ranges in which the pulsar has a dominant component, reducing the background to almost zero, while leaving high-energy events in the data set regardless of their pulse phase.

Thus, a future analysis, using more accurate models as well as an improved statistic may be able to find the exact extension of the inverse Compton radiation and therefore the form of the Crab nebula's energy population independent of its magnetic fields.

# Appendix

## Appendix A

The following derivations are taken from Rybicki & Lightman (1979, p. 167 et seqq. & p. 195 et seqq.).

When a charged particle is accelerated, it radiates electromagnetically. This is true regardless of the form of acceleration, be it actual momentum transfer to or from the particle or deflection. In the presence of a magnetic field, charged particles get accelerated by the Lorentz force:

$$F = q(E + v \times B)$$

with the charge  $q$ , the velocity  $v$ , and the electric and magnetic field strengths  $E, B$ .

With the absence of electric fields, the magnetic portion of the Lorentz force acts as a centripetal force, forcing the particle onto a circular (or spiral, in case of a parallel component) path. By setting the magnetic force equal to the centripetal force, the gyration frequency  $\omega_B$  of this circular motion is found to be:

$$\omega_B = \frac{qB}{\gamma m c}$$

with the particle mass  $m$ , the speed of light  $c$ , and the Lorentz-factor  $\gamma = E/(mc^2)$ .

The total radiated power, as mentioned in chapter 2.3.1, is:

$$P = \frac{2q^2}{3c^3} \gamma^4 (a_{\perp}^2 + \gamma^2 a_{\parallel}^2)$$

Thus, the total power emitted by a relativistic particle continuously accelerated by a magnetic field is:

## The Spatial Extension of the Inverse Compton Component of the Crab Nebula

### Appendix

---

$$P = \frac{2q^2}{3c^3} \gamma^4 \frac{q^2 B^2}{\gamma^2 m^2 c^2} v_{\perp} = \frac{2}{3} r_0^2 c \beta_{\perp} \gamma^2 B^2$$

For an isotropic distribution of particles, the particle speed  $\beta$  can be averaged to:

$$\langle \beta^2 \rangle = \frac{\beta^2}{4\pi} \int \sin^2 \alpha d\Omega = \frac{2\beta^2}{3}$$

which results in the total emitted power:

$$P = \left(\frac{2}{3}\right)^2 r_0^2 c \beta^2 \gamma^2 B^2 = \frac{4}{3} \sigma_T c \beta^2 \gamma^2 U_B$$

with the Thomson cross section  $\sigma_T = 8\pi r_0^2/3$  and the magnetic energy density  $U_B = B^2/8\pi$ .

The Compton effect occurs whenever a photon is scattered off an electron at rest. Since the photon carries momentum, the electron can recoil, gaining energy and momentum which the photon loses. The scattered photon therefore has a lower frequency than the incoming one. The energy of the photon  $\epsilon_1$  after scattering is:

$$\epsilon_1 = \frac{\epsilon}{1 + \frac{\epsilon}{mc^2}(1 - \cos \theta)}$$

with  $\epsilon$  the energy of the incoming photon.

It's wavelength is:

$$\lambda_1 - \lambda = \lambda_c (1 - \cos \theta)$$

with the Compton wavelength defined as:

$$\lambda_c \equiv \frac{h}{mc}$$

For electrons, it is  $\lambda_c(e^-) = 0.02426 \text{ \AA}$ .

In the rest frame of the electron, the Compton effect is always the same. In a different reference frame (the lab frame), in which the electron is highly relativistic, however, the momentum transfer may slow down the electron, resulting in a net energy transfer from the electron to the photon. This case is called the inverse Compton effect.

Let  $K$  be the lab frame, and  $K'$  be the electron rest frame. These two frames can be transformed into one another via a Doppler shift:

## The Spatial Extension of the Inverse Compton Component of the Crab Nebula

### Appendix

---

$$\epsilon' = \epsilon \gamma (1 - \beta \cos \theta)$$

and:

$$\epsilon_1 = \epsilon_1' \gamma (1 + \beta \cos \theta_1')$$

with  $\theta$ ,  $\theta_1$  the angle between the incoming, outgoing photon and the direction of the Doppler boost. If we assume maximum gain at  $\theta = \pi$  and  $\theta_1' = 0$  and inserting the formula, the energy for the photon in the lab frame  $\epsilon_1$  is:

$$\epsilon_1 = \frac{4\epsilon\gamma^2}{1 + \frac{2\epsilon\gamma}{mc^2}} \approx 4\epsilon\gamma^2$$

if  $\epsilon\gamma \ll mc^2$  holds. Since this approximation still holds true for photons of energies  $\sim 100$  keV, the inverse Compton effect can easily generate photons with energies  $> 1$  GeV, if they are scattered off electrons with a gamma of 100-1000.

The total power emitted for an isotropic distribution of photons off an isotropic distribution of electrons can be derived from the fact that  $\nu d\epsilon / \epsilon$  is a Lorentz invariant (see Rybicki & Lightman 1979 p. 199), where  $\nu d\epsilon$  is the density of photons in the energy range  $d\epsilon$ . The total power emitted in the electron rest frame is:

$$\frac{dE_1}{dt'} = c\sigma_T \int \epsilon_1' \nu' d\epsilon'$$

Assuming that the energy change in the rest frame is much smaller than that in the lab frame, one can set  $\epsilon_1' = \epsilon'$ . From the invariance of emitted power, it also follows that  $dE_1/dt = dE_1'/dt'$ . The energy loss in the lab frame is thereby:

$$\frac{dE_1}{dt} = c\sigma_T \int \epsilon'^2 \frac{\nu' d\epsilon'}{\epsilon'} = c\sigma_T \int \epsilon'^2 \frac{\nu d\epsilon}{\epsilon}$$

Inserting the photon energy  $\epsilon'$ , this becomes:

$$\frac{dE_1}{dt} = c\sigma_T \int (1 - \beta \cos \theta)^2 \epsilon \nu d\epsilon$$

For an isotropic distribution of photons:

$$\langle (1 - \beta \cos \theta)^2 \rangle = 1 + \frac{1}{3} \beta^2$$

## The Spatial Extension of the Inverse Compton Component of the Crab Nebula

### Appendix

---

since  $\langle \cos x \rangle = 0$  and  $\langle \cos x^2 \rangle = 1/3$ . The total emitted power becomes:

$$\frac{dE_{rad}}{dt} = c \sigma_T U_{ph} \left[ \gamma^2 \left( 1 + \frac{1}{3} \beta^2 \right) - 1 \right]$$

which uses the initial photon energy density as:

$$U_{ph} \equiv \int \epsilon \nu d\epsilon$$

and also accounts for the initial photon absorption, which, in respect to the power emitted by the electron, is:

$$\left( \frac{dE_1}{dt} \right)_{abs} = -c \sigma_T \int \epsilon \nu d\epsilon = -\sigma_T c U_{ph}$$

Finally, using the relation  $\gamma^2 - 1 = \gamma^2 \beta^2$ , the total power emitted through inverse Compton radiation is:

$$P_{compt} = \frac{dE_{rad}}{dt} = \frac{4}{3} \sigma_T c \gamma^2 \beta^2 U_{ph}$$

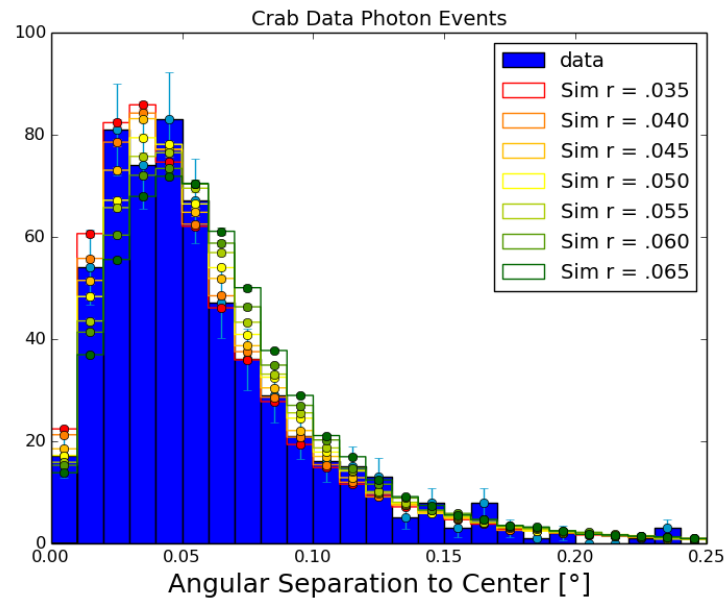
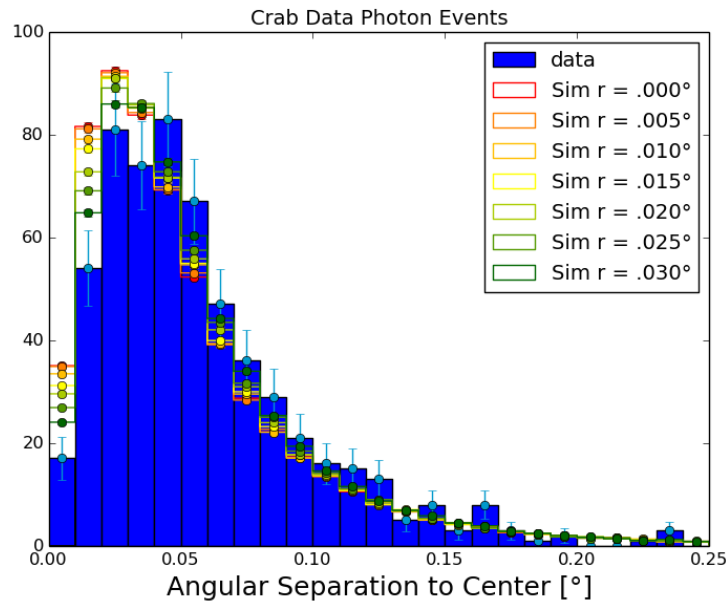
Which is almost identical to the emitted synchrotron power save for one factor. Finally, their quotient reduces to:

$$\frac{P_{synch}}{P_{compt}} = \frac{U_B}{U_{ph}}$$

## Appendix B

These are the complete histograms for all model template from smallest (red) to largest (green).

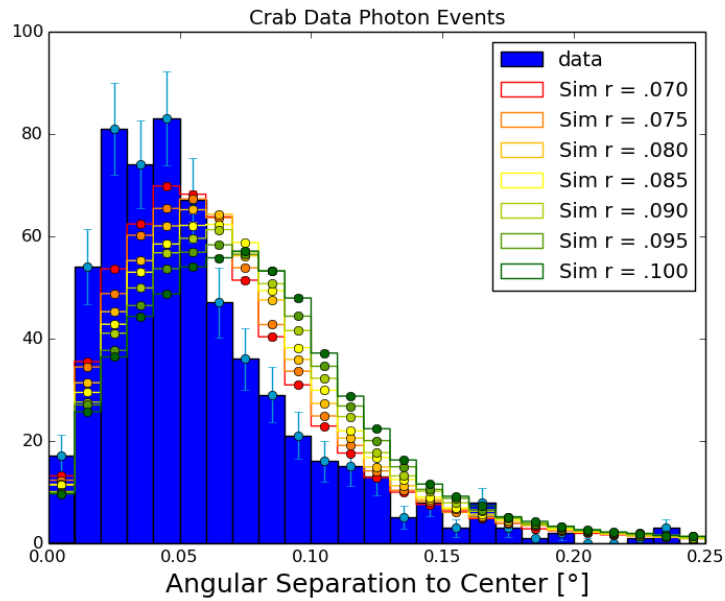
For the full Crab data:



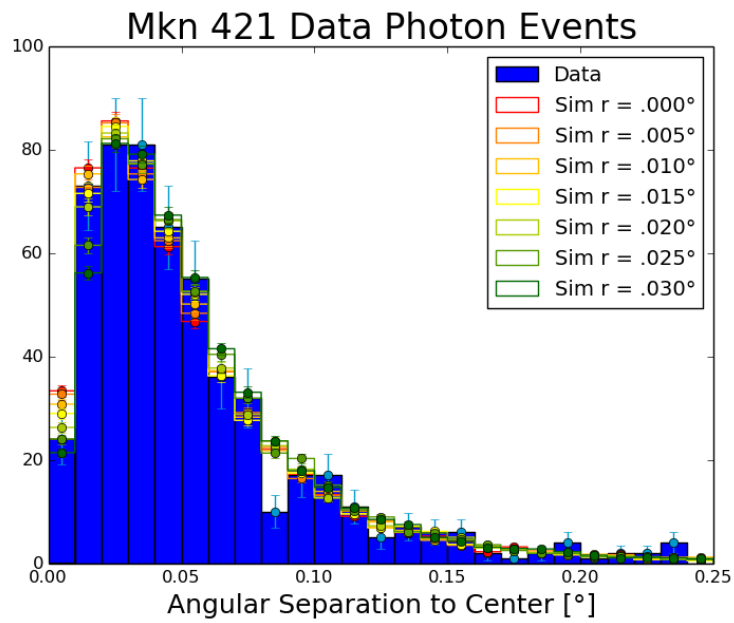
# The Spatial Extension of the Inverse Compton Component of the Crab Nebula

## Appendix

---



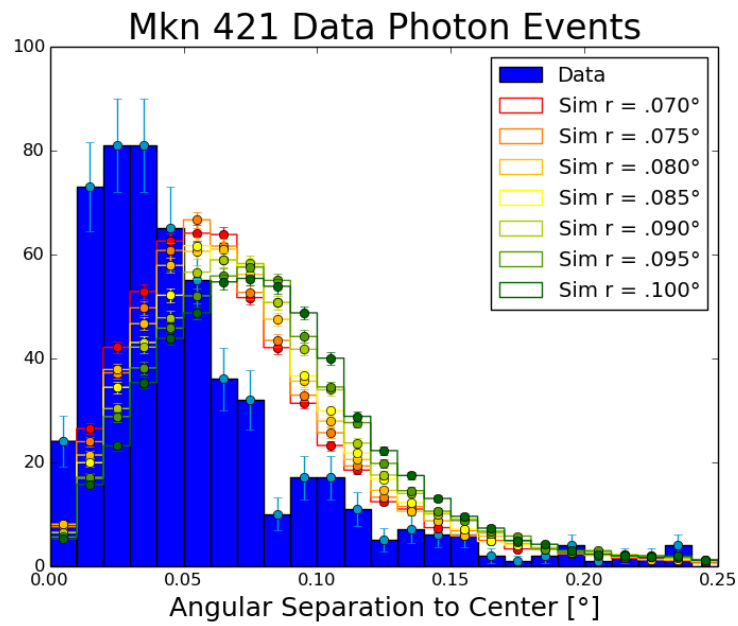
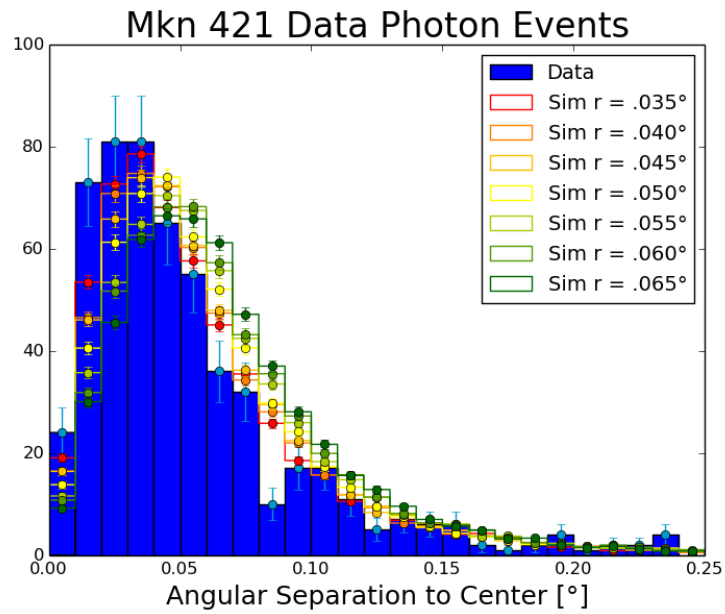
For the Mkn 421 data:



# The Spatial Extension of the Inverse Compton Component of the Crab Nebula

Appendix

---

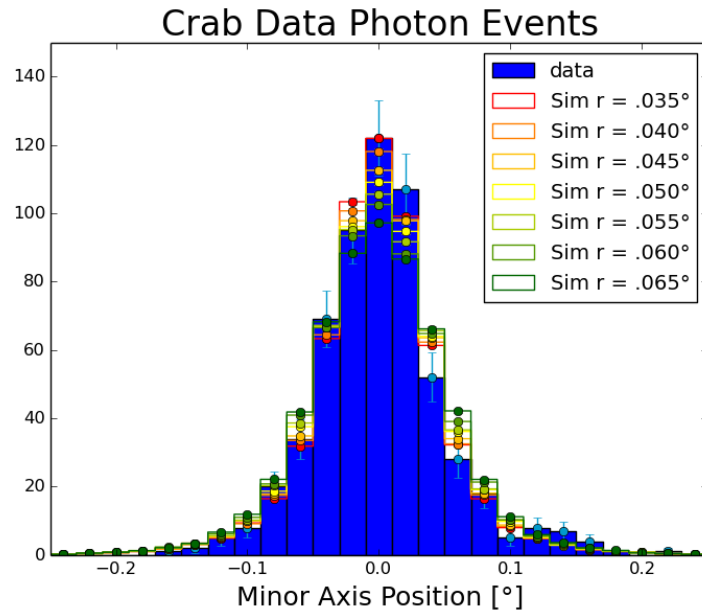
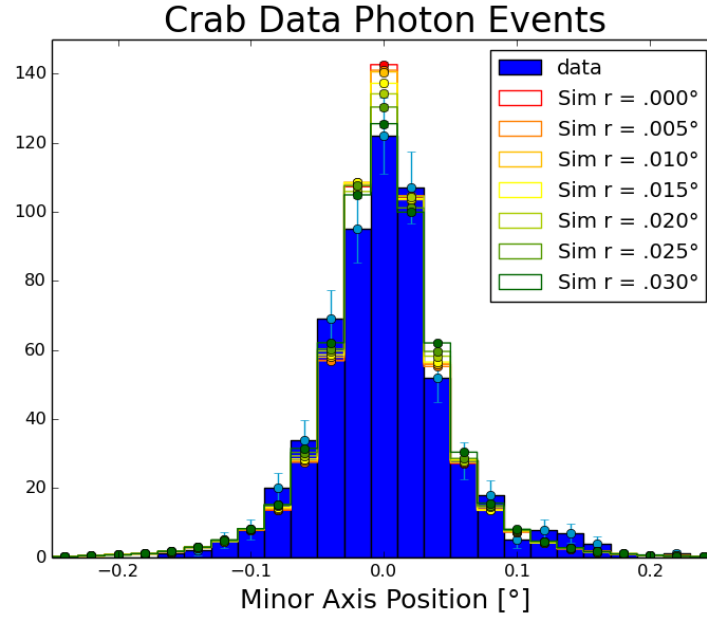


# The Spatial Extension of the Inverse Compton Component of the Crab Nebula

Appendix

---

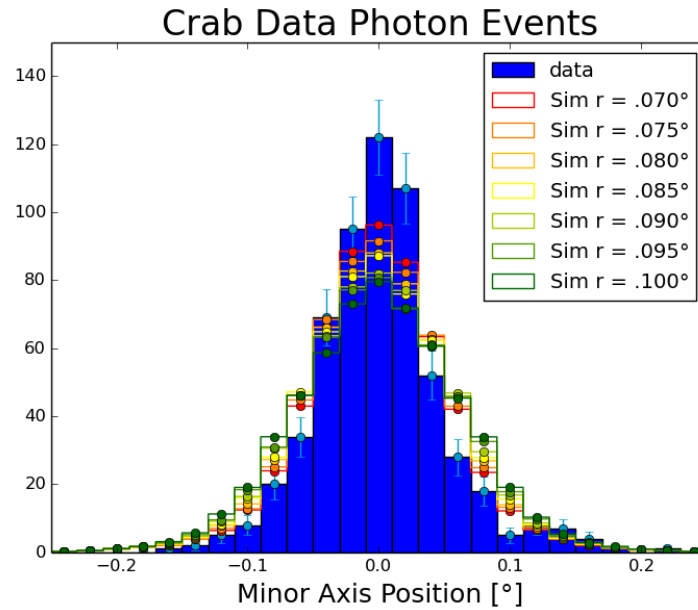
For the Crab minor axis:



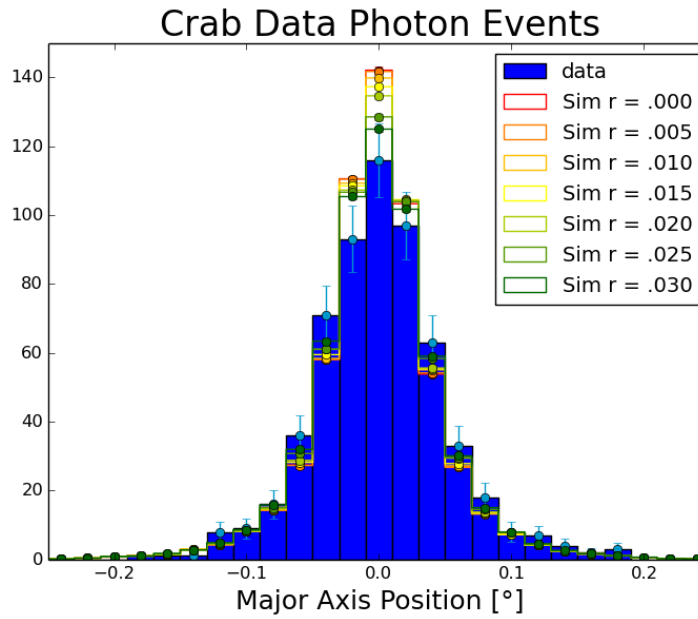
# The Spatial Extension of the Inverse Compton Component of the Crab Nebula

Appendix

---



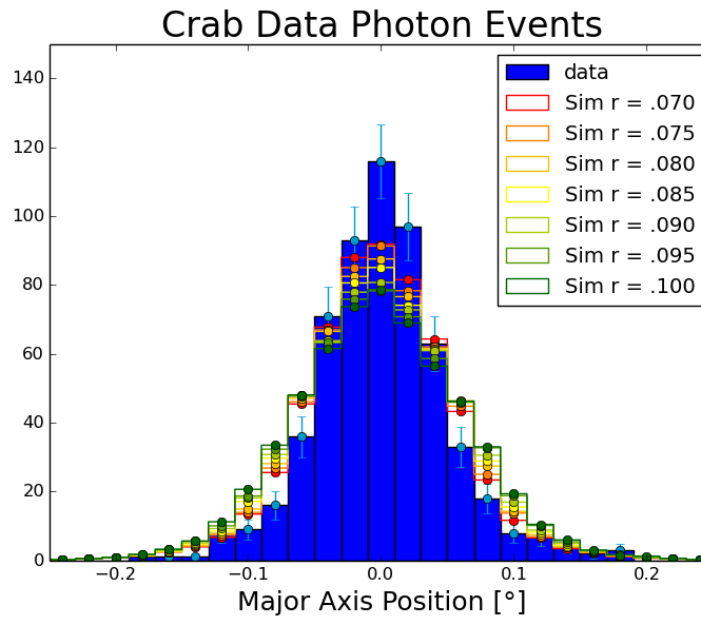
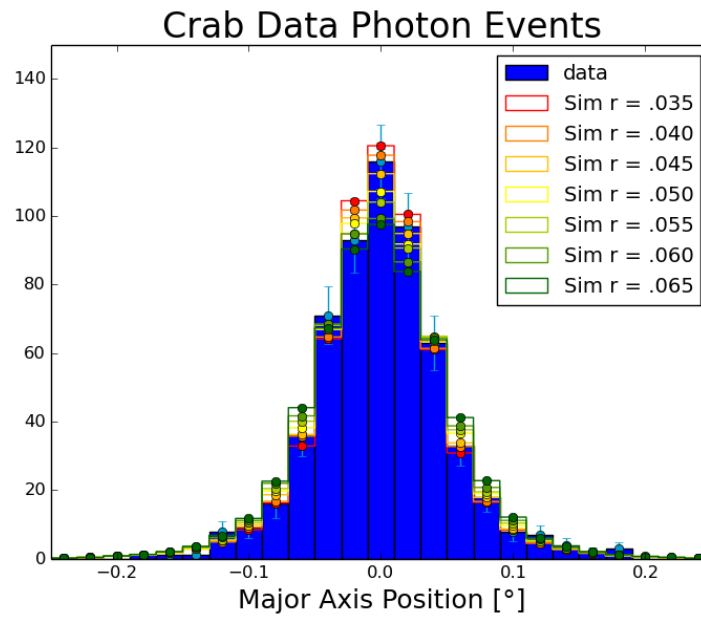
For the Crab major axis:



# The Spatial Extension of the Inverse Compton Component of the Crab Nebula

*Appendix*

---



# The Spatial Extension of the Inverse Compton Component of the Crab Nebula

## Appendix

---

### List of Figures

Figure 2.1: Composite image of the Crab nebula.....	4
Figure 2.2: Crab pulsar phase.....	6
Grafik1.....	10
Figure 3.1: Cross section of Fermi LAT.....	15
Figure 3.2: Full converter-tracker array.....	17
Figure 3.3: Opened converter-tracker module.....	18
Figure 3.4: Converter-tracker design principle.....	19
Figure 3.5: PSF of conversion types.....	22
Figure 3.7: 95% containment radius of PSF classes.....	23
Figure 3.6: 68% containment radius of PSF classes.....	23
Figure 4.1: Crab data phasogram.....	28
Figure 4.2: Conversion type by PSF type.....	30
Figure 4.3: Containment of simulated photon inside $0.25^\circ$ radius.....	32
Figure 4.4: Simulated PSFs for all PSF classes.....	33
Figure 4.5: Simulated PSFs for combined PSF classes.....	33
Figure 4.6: Background events in $0.25^\circ$ radius.....	35
Figure 4.7: Signal Events in $0.25^\circ$ radius.....	35
Figure 4.8: Crab data phasogram at energies $> 18$ GeV.....	38
Figure 5.1: Angular separation of Crab data.....	42
Figure 5.2: Likelihood Crab data.....	44
Figure 5.3: Angular separation of Mkn 421 data.....	46
Figure 5.4: Likelihood Mkn 421 data.....	46
Figure 5.5: Angular separation of $r < 0.05^\circ$ Mkn 421 data.....	48
Figure 5.6: Angular separation of $r < 0.10^\circ$ Mkn 421 data.....	48
Figure 5.7: Likelihood $r < 0.05^\circ$ Mkn 421 data.....	49
Figure 5.8: Likelihood $r < 0.10^\circ$ Mkn 421 data.....	49
Figure 5.9: Angular separation of Mkn 421 PSF2-only data.....	50
Figure 5.10: Angular separation of Mkn 421 PSF3-only data.....	50
Figure 5.11: Likelihood Mkn 421 PSF2-only data.....	51
Figure 5.12: Likelihood Mkn 421 PSF3-only data.....	51
Figure 5.13: Direct comparison between Crab data and Mkn 421 data.....	53
Figure 5.14: Crab photon distribution along its minor axis.....	57
Figure 5.15: Crab photon distribution along its major axis.....	57
Figure 5.16: Likelihood Crab minor axis distribution.....	58
Figure 5.17: Likelihood Crab major axis distribution.....	58
Figure A2: Crab angular separation medium templates.....	65
Figure A1: Crab angular separation small templates.....	65
Figure A3: Crab angular separation large templates.....	66
Figure A4: Mkn 421 angular separation small templates.....	66
Figure A5: Mkn 421 angular separation medium templates.....	67

# The Spatial Extension of the Inverse Compton Component of the Crab Nebula

## *Appendix*

---

Figure A6: Mkn 421 angular separation large templates.....	67
Figure A7: Crab minor axis small templates.....	68
Figure A8: Crab minor axis medium templates.....	68
Figure A9: Crab minor axis large templates.....	69
Figure A10: Crab major axis small templates.....	69
Figure A11: Crab major axis medium templates.....	70
Figure A12: Crab major axis large templates.....	70

# Bibliography

**Abdo, A.A. et al.:** *Fermi-LAT Observations of Markarian 421: the Missing Piece of its Spectral Energy Distribution.* arXiv:1106.1348v1 [astro-ph.HE]}, 2011

**Aharonian, F.A. et al.:** *First ground based measurement of atmospheric Cherenkov light from cosmic rays.* In: Physical Review D 75:042004, 2007

**Aleksic, J. et al.:** *Phase-resolved energy spectra of the Crab pulsar in the range of 50–400 GeV measured with the MAGIC telescopes.* In: Astronomy and Astrophysics 540, A69, <http://dx.doi.org/10.1051/0004-6361/201118166>}, 2012.

**Atwood, W.B. et al.:** *The Large Area Telescope on the Fermi Gamma-ray Space Telescope Mission.* In: The Astrophysical Journal 697:1071-1102, 2009

**Atwood, W.B.; Baldini, L.; Bruel, P.; Caputo, R.; Sgro, C.:** *Improving the Scientific Potential of Pass 8: Status and Plans for a future Pass 8 Release.* URL: Improving the Scientific Potential of Pass 8: Status and Plans for a future Pass 8 Release, 2016.

**Bartoli, B. et al.:** *4.5 years multi-wavelength observations of Mrk 421 during the ARGO-YBJ and Fermi common operation time.* In: The Astrophysical Journal Supplement Series 222, arXiv:1511.06851v1 [astro-ph.HE]}, 2015

# The Spatial Extension of the Inverse Compton Component of the Crab Nebula

## Bibliography

---

**Bühler, Rolf:** *Gamma-ray Activity in the Crab Nebula: The Exceptional Flare of April 2011.* In: The Astrophysical Journal, Volume 749, Issue 1, article id. 26, 8 pp., [arXiv:1112.1979v2](https://arxiv.org/abs/1112.1979v2) [astro-ph.HE], 2011

**Bühler, Rolf; Blandford, Roger:** *The surprising Crab pulsar and its nebula: A review.* In: Reports on Progress in Physics, Volume 77, Issue 6, article id. 066901, arXiv:1309.7046 [astro-ph.HE], 2014.

**P. Carlson et al.:** *Long narrow CsI(Tl) rods as calorimeter elements.* In: Nuclear Instruments and Methods A376 271, 1996

**Chen, Wenley; Buckley, James H.; Ferrer, Francesc:** Search for GeV  $\gamma$ -Ray Pair Halos Around Low Redshift Blazars. In: Phys. Rev. Lett. **115**, 211103, 2015

**Cocke, W.J.; Disney, M.J.; Taylor, D.J.:** *Discovery of Optical Signals from Pulsar NP 0532.* In: Nature, Volume 221, Issue 5180, pp. 525-527, 1969

**FERMI.** URL: [fermi.gsfc.nasa.gov/ssc/data/access/lat/4yr\\_catalog/](https://fermi.gsfc.nasa.gov/ssc/data/access/lat/4yr_catalog/), 2016

**FSSC.** URL: [fermi.gsfc.nasa.gov/ssc/data/access/lat/](https://fermi.gsfc.nasa.gov/ssc/data/access/lat/), 2016

**Harding, Alike K.:** *The neutron star zoo.* In: Frontiers of Physics, Volume 8, Issue 6, pp.679-692, 2013.

## The Spatial Extension of the Inverse Compton Component of the Crab Nebula

### Bibliography

---

**Hester, JJ:** *The Crab Nebula: An Astrophysical Chimera*, In: Annual Review of Astronomy and Astrophysics Vol. 46: 127-155, 2008.

**Lyne, A. G., Pritchard, R. S., & Graham-Smith, F.:** *Twenty-Three Years of Crab Pulsar Rotational History*. In: Monthly Notices of the Royal Astronomical Society, Vol. 265, NO. 4/DEC15, P.1003, 1993

**Mayer, M. et al.:** *Rapid Gamma-Ray Flux Variability During the 2013 March Crab Nebula Flare*. In: The Astrophysical Journal 775(2), L37, 2013

**PAC - Pierre Auger Collaboration:** *Muons in air showers at the Pierre Auger Observatory: Mean number in highly inclined events*. In: Phys. Rev. D 91, 032003, 2015

**Porth, Oliver; Komissarov, Serguei S.; Keppens, Rony:** *Solution to the Sigma-Problem of Pulsar Wind Nebulae*. [arXiv:1212.1382v1](https://arxiv.org/abs/1212.1382v1) [astro-ph.HE], 2012

**Roe, Byron P.:** *Probability and Statistics in Experimental Physics*. New York: Springer, 1992

**Rybicki, George B.; Lightman, Alan P.:** *Radiative Processes in Astrophysics*. Weinheim: WILEY-VCH, 2004, ISBN-10: 0-471-82759-2

**SLAC.** URL: [www.slac.stanford.edu/exp/glast/groups/canda/lat\\_Performance.htm](http://www.slac.stanford.edu/exp/glast/groups/canda/lat_Performance.htm), 2016

**Tavani, M. et al.:** Discovery of Powerful Gamma-Ray Flares from the Crab Nebula. In: Science 11 Feb 2011: Vol. 331, Issue 6018, pp. 736-739, DOI: 10.1126/science.1200083

**The Spatial Extension of the Inverse Compton Component of the Crab Nebula**  
*Bibliography*

---

# The Spatial Extension of the Inverse Compton Component of the Crab Nebula

---

## Erklärung:

Hiermit bestätige ich, dass die vorliegende Arbeit von mir selbständig verfasst wurde und ich keine anderen als die angegebenen Hilfsmittel – insbesondere keine im Quellenverzeichnis nicht benannten Internet-Quellen – benutzt habe und die Arbeit von mir vorher nicht einem anderen Prüfungsverfahren eingereicht wurde. Die eingereichte schriftliche Fassung entspricht der auf dem elektronischen Speichermedium. Ich bin damit einverstanden, dass die Masterarbeit veröffentlicht wird.

---

Ort, Datum

---

Unterschrift